nature immunology

Article

https://doi.org/10.1038/s41590-026-02421-w

Metabolic quiescence of naive-like memory T cells precedes and maintains antigen-specific T cell memory

Received: 11 May 2025

Accepted: 7 January 2026

Sina Frischholz[1,15], Ev-Marie Schuster[1,15], Myriam Grotz[1,15], Christine Schülein[1], Julia Benz[1], Katharina Kocher[1], Lucia Klotz[1], Szilard Varga[2,3], Theresa Hiltner[4], Rayya Alsalameh[1], Jan Esse[1], Johannes Träger[1], Jürgen Held[1], Frederik Graw[2,5], Jürgen Pahle[3], Bernd Spriewald[2], Luca Gattinoni[6,7,8], Veit R. Buchholz[4,9], Felix Drost[10], Benjamin Schubert[10], Simon Rothenfußer[11,12], Dirk H. Busch[4,13], Christian Bogdan[1,14] & Kilian Schober[1,14] ✉

Metabolic activity shapes cell fate but remains challenging to capture in vivo with high resolution. Here we performed longitudinal metabolic and phenotypic profiling of human antigen-specific $CD8^+$ T cells after yellow fever vaccination using flow cytometry and single-cell RNA sequencing. As assessed by protein translation rates, $CD8^+$ T cells upregulated glycolysis to fuel anabolic needs for proliferation but predominantly used oxidative phosphorylation for energy production during the acute phase (days 7–28) after vaccination. Simultaneously, $CD8^+CD62L^+CD45RA^-$ central memory T cells were the most metabolically active subset, whereas $CD8^+CD62L^-CD45RA^+$ effector T cells underwent metabolic shutdown. Weakly differentiated $CD8^+CD62L^+CD45RA^+CD95^-$ naive-like memory T cells showed minimal activity, relied solely on oxidative phosphorylation and were preferentially maintained 26 years postvaccination, reinforcing the link between cellular quiescence and longevity. Our study highlights quiescence as a key feature for long-term immunological memory formation in humans.

The metabolic dynamics of antigen-specific $CD8^+$ T cells in humans remain poorly understood. After activation, naive T (T_N) cells give rise to antigen-experienced subsets including naive-like memory (T_{NM}), stem cell memory (T_{SCM}), central memory (T_{CM}), effector memory (T_{EM}) and effector (T_E) T cells. Antigen-experienced T_{NM} cells thereby differ from antigen-inexperienced T_N cells through cellular abundance and enhanced recall capacity and form a dominant memory T cell subset following yellow fever or smallpox vaccination[1–3]. T_{EM} and T_E cells dominate the acute phase but can persist for years after antigen encounter[1–5]. Studies, mostly in mice, suggest that persisting memory T cells arise from acute-phase precursors expressing CD62L or TCF-1[6,7], typically T_{CM} cells in mice and T_{NM} and/or T_{SCM} cells in humans). These T cells also respond to secondary antigen challenge[8,9]. By contrast, T_{EM} and T_E cells contract after the acute phase[10–12], a process linked to higher proliferation speeds[13] and accumulation of cell divisions[8]. This suggests that quiescence, a hallmark of T_N cells[14], may also characterize early-differentiated antigen-experienced memory precursors[15]. Experimental evidence for this in vivo remains scarce, especially in humans.

The bioenergetic demands of T cells are mainly fueled through glycolysis or oxidative phosphorylation (OXPHOS)[15]. T cells become metabolically active and increase glycolysis after in vitro activation, whereas resting T cells are quiescent, feeding on mitochondrial respiration[16–19].

A full list of affiliations appears at the end of the paper. ✉e-mail: kilian.schober@uk-erlangen.de

Mouse T cells activated in vivo maintain high dependence on OXPHOS even during the acute phase of an immune response[20,21]. Genetic knockouts in mice allow more mechanistic investigation compared to studies in humans[22–24] but have led to conflicting observations on the interplay of metabolism and T cell memory: elevated glycolysis leads to accelerated differentiation of T_{CM} into T_{EM} cells, yet functional memory T cells are retained despite decreased OXPHOS[22,24]. Conversely, differentiation of memory T cells is enhanced by inhibition of glycolysis through 2-deoxy-D-glucose (2-DG)[23].

Here we analyzed metabolic profiles of in vivo activated human antigen-specific T cells at high resolution. T_{CM} cells were most metabolically active, relying mostly on OXPHOS, but they also used glycolysis. T_{EM} and T_E cells underwent metabolic shutdown, whereas T_{NM} cells remained quiescent throughout the immune response, emerging as the dominant memory subset after antigen clearance.

Results

T_{NM} cells persist after YFV vaccination

We analyzed the $CD8^+$ T cell response in 68 healthy volunteers (age 20–62 years; 26 males, 42 females) who received the live-attenuated yellow fever virus (YFV) vaccine YF-17D once; this vaccine, in immunocompetent vaccinees[25,26], induces long-lasting immunity[1,27]. Using flow cytometry and single-cell RNA sequencing (scRNA-seq), we studied $CD8^+$ T cells from blood at days 7, 11, 14, 21, 28, 49, 90 and 365, covering acute (day 7–28) and memory (day 49–365) phases (Fig. 1a). We also included blood samples from three unvaccinated donors (age 28–61 years, 1 male, 2 females) and from five donors vaccinated 7–26 years ago (age 25–55 years, 1 male, 4 females) (Supplementary Table 1). T cells were analyzed after cryopreservation or in fresh whole blood (Extended Data Fig. 1a).

Antigen-specific $CD8^+$ T cells were identified with fluorophore-conjugated peptide human leukocyte antigen (pHLA) multimers targeting the immunodominant HLA-A2-restricted YFV epitope $NS4B_{214}$ (A2/NS4B) using flow cytometry[28]. The frequency of A2/$NS4B^+CD8^+$ T cells peaked at day 14–49 and remained detectable 26 years after a single immunization (Fig. 1b). Absolute A2/$NS4B^+CD8^+$ cell numbers ranged from 10^1 to 10^4 per milliliter of blood (Extended Data Fig. 1b). We refer to antigen-inexperienced $CD62L^+CD45RA^+CD95^-$ cells as T_N (prevaccination), and to antigen-experienced $CD62L^+CD45RA^+CD95^-$ cells as T_{NM} (postvaccination)[1,2]. At day 7–14, $CD62L^+CD45RA^-$ T_{CM} and $CD62L^-CD45RA^-$ T_{EM} subsets were most prominent; from day 90 to year 7–26, the proportion of $CD62L^+CD45RA^+CD95^-$ T_{NM} cells increased (Fig. 1c,d). Flow cytometric analysis of whole blood yielded distributions of T_{NM} and $CD62L^-CD45RA^+$ T_E similar to those of cryopreserved cells, although at day 11–21 T_{CM} were more frequent (>50% of all) than T_{EM} cells in whole blood compared to cryopreserved cells (Extended Data Fig. 1c–f). Using CCR7 instead of CD62L to stain for T_{NM}, T_{SCM} and T_{CM} indicated that $CCR7^+CD45RA^-$ T_{CM} and $CCR7^-CD45RA^-$ T_{EM} cells dominated the acute response (>70%), whereas at day 90–365 $CCR7^+CD45RA^+CD95^-$ T_{NM} cells became more frequent (>20–40%) (Extended Data Fig. 1e–g).

We also performed scRNA-seq with T cell receptor (TCR) sequencing and cellular indexing of transcriptomes and epitopes by sequencing (CITE-seq) with the same surface protein markers as those used for flow cytometry on cryopreserved samples from 26 donors, selected from the cohorts introduced above based on matching HLA (3 unvaccinated donors, 5 long-term vaccinated donors, and 18 recently vaccinated donors aged 21–55 years, 8 males and 10 females), spanning day 0 to 26 years postvaccination (Fig. 1e). We used DNA-barcoded pHLA multimers (dextramers) for eight YFV epitopes[29] and five control epitopes from SARS-CoV-2, HHV-1, influenza virus and Epstein–Barr virus (Supplementary Table 3). Each dextramer contained a fluorochrome for enrichment by fluorescence-activated cell sorting (Supplementary Fig. 1a). Across three scRNA-seq experiments, we recovered 29,968 cells (Fig. 1f, Extended Data Fig. 1h and Supplementary Table 4). A2/NS4B-specific T cells were particularly identified in *MKI67*^{hi} cycling, *SELL*^{hi} T_N/T_{NM}, *IL7R*^{hi} T_{CM} and *GZMK*^{hi} T_{EM} or *CCL5*^{hi} T_E cells, with or without an interferon (IFN)-sensing signature (Extended Data Fig. 1i–k and Supplementary Table 5).

We assigned epitope specificities using an algorithm that integrates dextramer clone purity, cell purity and unique molecular identifier (UMI) counts and was validated by TCR reexpression (Supplementary Fig. 1b,c). Apart from A2/NS4B-specific T cells (6,247 cells) and control virus-specific T cells, we identified $CD8^+$ T cells specific for four less immunodominant YFV epitopes ($NS2A_{97}$, $NS2B_{117}$, $NS3_{286}$, $NS3_{292}$; Supplementary Fig. 1d,e). On a transcriptional level, most A2/$NS4B^+CD8^+$ T cells were in T_N/T_{NM} clusters at day 0 (representing antigen-inexperienced T_N cells), with cells transitioning to T_{CM}, T_{EM} and the cycling cluster at day 11–14 (Fig. 1g,h). By day 21–90, cells gradually shifted toward IFN T_{EM}/IFN T_E clusters, and, after 1 year, more cells were found in the T_N/T_{NM} clusters (Fig. 1g,h and Extended Data Fig. 1l,m).

CITE-seq identified $CD62L^+CD45RA^+CD95^+$ T_{SCM} and $CD62L^-CD45RA^-$ T_{EM} cells across all transcriptional clusters (Fig. 1h and Supplementary Fig. 2a–c) that partly overlapped with published[30] transcriptional states for sorted subsets (Supplementary Fig. 2d). $CD62L^+CD45RA^+CD95^-$ T_N/T_{NM} cells mainly mapped to *SELL*^{hi} T_N/T_{NM} clusters. Cycling cells mainly possessed a $CD62L^+CD45RA^-$ T_{CM} and $CD62L^-CD45RA^-$ T_{EM} phenotype (Supplementary Fig. 2b). As the CCR7 signal was weak in the CITE-seq data, whereas CD62L was reliably detected by flow cytometry and CITE-seq (Supplementary Fig. 2a), we used CD62L as a marker. CD62L shedding occurs owing to stress and/or activation[31]. We found fewer T_{NM}, T_{SCM} and T_{CM} cells after cryopreservation compared to those in fresh whole blood (day 11–28), and CD62L expression was reduced compared to CCR7 positivity only at day 7 (Extended Data Fig. 1e–g), suggesting that CD62L shedding occurred in cryopreserved samples early after vaccination. $CD62L^-CD45RA^-$ T_{EM} or $CD62L^-CD45RA^+$ T_E cell classification aligned with transcriptional *GZMK*^{hi} T_{EM} and *CCL5*^{hi} T_E clusters (Supplementary Fig. 2c). In an

Fig. 1 | T_{NM} cells persist after YFV vaccination. **a**, Study design showing $n = 3$ unvaccinated donors; $n = 4$ to $n = 58$ volunteers vaccinated with YF-17D at day 0 followed by blood sampling at days 7, 11, 14, 21, 28, 49, 90 and 365; and $n = 5$ donors vaccinated 7–26 years ago. **b**, Representative flow cytometry plots at days 0, 14 and 365 (left) and quantification at time points as in **a** (right) of A2/$NS4B^+CD8^+$ T cells from vaccinated donors (see Supplementary Table 2 for donor distribution across panels). The line represents the mean and the gray area the s.e.m. **c**, Distribution of A2/$NS4B^+CD8^+$ T cells ($CD62L^+CD45RA^+CD95^-$ T_{NM}, $CD62L^+CD45RA^+CD95^+$ T_{SCM}, $CD62L^+CD45RA^-$ T_{CM}, $CD62L^-CD45RA^-$ T_{EM}, $CD62L^-CD45RA^+$ T_E cells) at days 14 and 365 by flow cytometry. The line indicates the median; $n = 20$ to $n = 38$ donors per time point. Statistics: two-way analysis of variance (ANOVA) with Šídák's multiple comparisons test. **d**, Representative flow cytometry plots (left) and quantification (right) of A2/$NS4B^+CD8^+$ T_{NM}, T_{SCM}, T_{CM}, T_{EM} and T_E cells as in **c**. Bars indicate the mean and s.e.m.; $n = 3$ to $n = 38$ donors per time point (as in **a**). **e**, Quantification of A2/$NS4B^+CD8^+$ T_{NM}, T_{SCM}, T_{CM}, T_{EM} and T_E cells as in **c** based on CITE-seq. Bars indicate the mean and s.e.m. $n = 3$ to $n = 12$ donors per time point (as in **a**). **f**, UMAP of scRNA-seq data (left) and quantification at time points as in **a** (right) with Leiden clusters of $CD8^+$ T cells enriched for A2/$NS4B^+$ cells by flow cytometry ($n = 29{,}968$ cells); $n = 3$ to $n = 12$ donors per time point. **g**, UMAP (left) and quantification at time points as in **a** (right) of pseudotime of $CD8^+$ T cells as in **f**. Pseudotime origin set in *SELL*^{hi} T_N/T_{NM} clusters; color gradient clipped at 0.5. **h**, UMAP of A2/$NS4B^+CD8^+$ T_{NM}, T_{SCM}, T_{CM}, T_{EM} and T_E cells based on CITE-seq as in **e**. A2/$NS4B^+CD8^+$ cells were enriched by MACS before fluorescence-activated cell sorting at day 0 and 7–26 years postvaccination. Gray, A2/$NS4B^-CD8^+$ T cells. Gini index (GI), number of clones (C), and number of cells (n) for A2/$NS4B^+CD8^+$. **i**, UMAP of A2/$NS4B^+CD8^+$ T cells at day 0 in 3 donors (A7, A21, A33) and 7–26 years postvaccination in 5 donors (C15, C11, C7, C12, C5). Colors represent cells with the indicated clone size for each donor. Gray, A2/$NS4B^-CD8^+$ T cells.

independent scRNA-seq dataset[32] with 130 CITE-seq markers, CD45RA and CD62L emerged as top predictors of *SELL*^{hi} T_N/T_{NM} transcriptional profiles (Supplementary Fig. 2e). Therefore, CD62L surface protein is a meaningful marker for T_{NM}, T_{SCM} and T_{CM} cells.

TCR repertoire analysis indicated that A2/NS4B$^+$CD8$^+$ antigen-inexperienced cells at day 0 exhibited low clonality and a low Gini index (Fig. 1h), suggesting high diversity. The Gini index peaked at day 28 owing to clonal expansion (Supplementary Fig. 2f). Seven to 26 years after vaccination, A2/NS4B$^+$CD8$^+$ clones consisted of one or two CD8$^+$ T cells, except for a single clone that comprised 66 cells (Fig. 1i). These findings indicate that human antigen-specific CD8$^+$ T cell memory to YFV is characterized by stem-like T_{NM} cells with polyclonal TCR repertoires.

T_{CM} cells are metabolically most active

Surface expression of activation markers HLA-DR and CD38 was highest at day 14–21 (Fig. 2a and Extended Data Fig. 2). To characterize qualitative features of the T cell response, we analyzed the metabolic

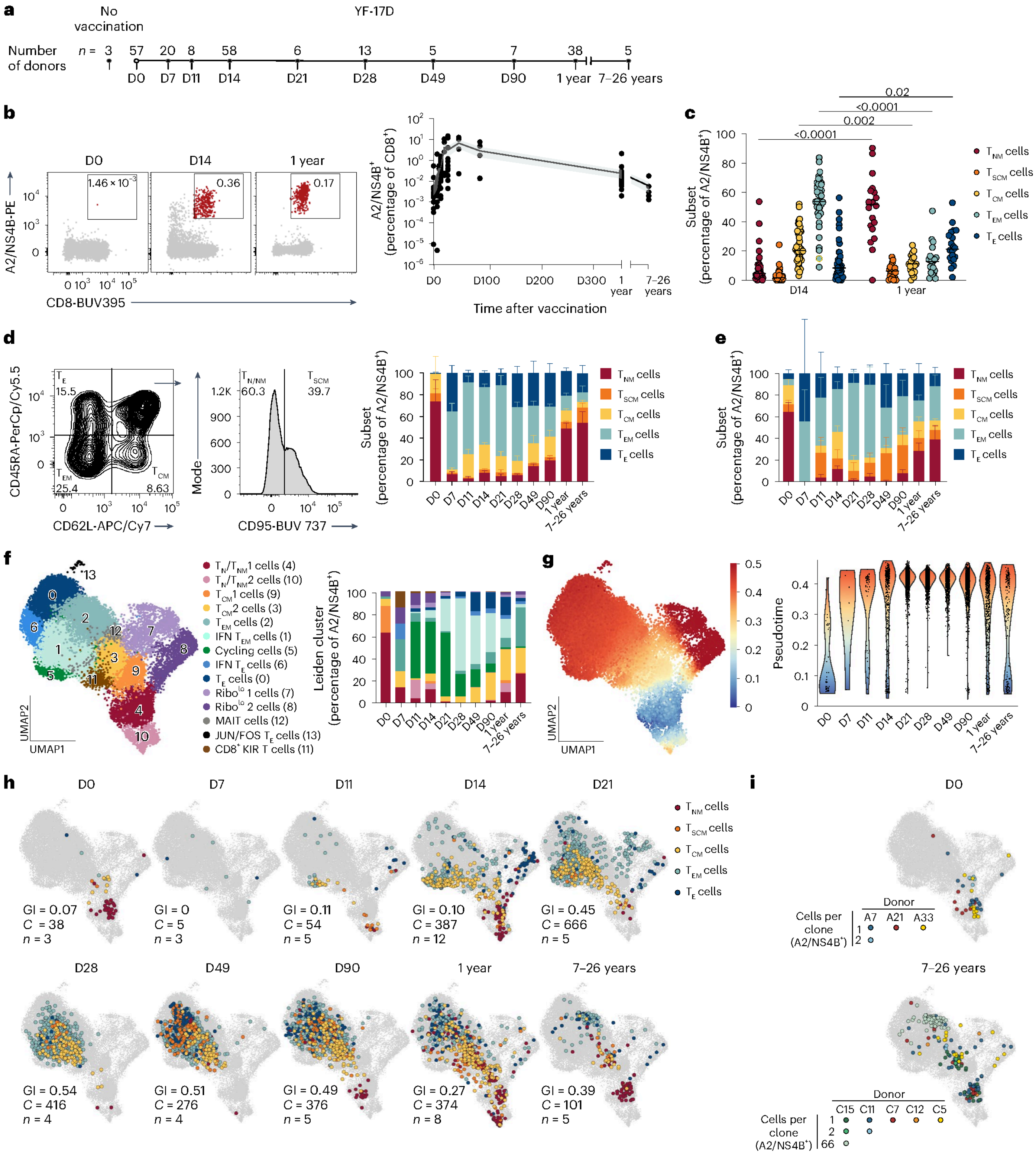

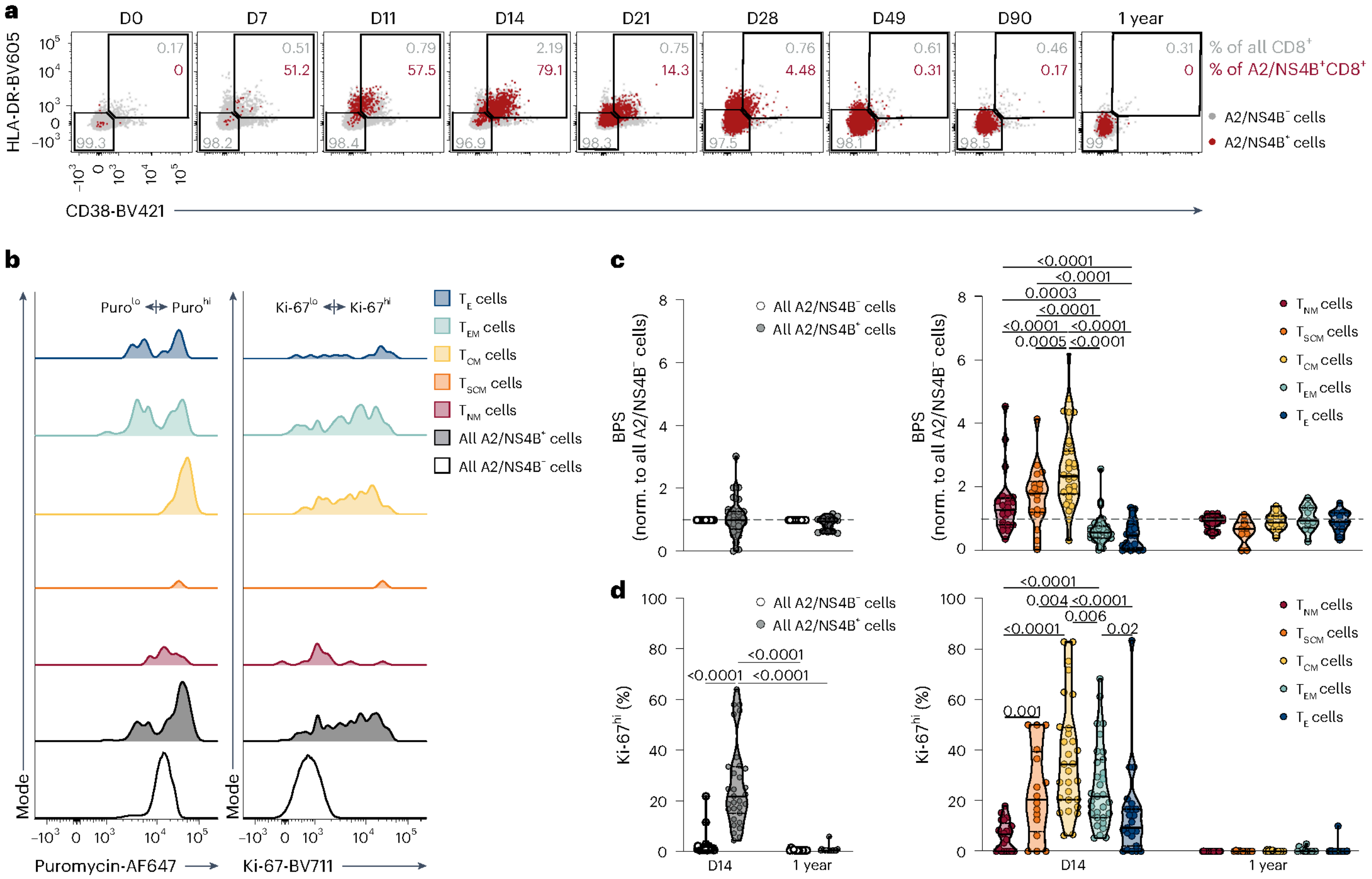

Fig. 2 | T_{CM} cells are metabolically most active. **a**, Representative flow cytometry plots for HLA-DR and CD38 expression of CD8$^+$ T cells after YFV vaccination (pregated on living, CD19$^-$CD56$^-$CD4$^-$CD3$^+$CD8$^+$ lymphocytes). Red, A2/NS4B$^+$CD8$^+$ T cells; gray, A2/NS4B$^-$CD8$^+$ T cells. Red text indicates the percentage of HLA-DR$^+$CD38$^+$ cells among A2/NS4B$^+$CD8$^+$ T cells and gray text the percentage of HLA-DR$^+$CD38$^+$ cells among CD8$^+$ T cells. **b**, Representative histograms for flow cytometry analysis of puromycin incorporation (left) and Ki-67 expression (right) in A2/NS4B$^-$CD8$^+$, A2/NS4B$^+$CD8$^+$ and A2/NS4B$^+$CD8$^+$ T cell subsets (CD62L$^+$CD45RA$^+$CD95$^-$ T_{NM}, CD62L$^+$CD45RA$^+$CD95$^+$ T_{SCM}, CD62L$^+$CD45RA$^-$ T_{CM}, CD62L$^-$CD45RA$^-$ T_{EM}, CD62L$^-$CD45RA$^+$ T_E cells) at day 14 post-YFV vaccination. **c**, Flow cytometry analysis of BPS rates of all A2/NS4B$^-$ and A2/NS4B$^+$CD8$^+$ T cells (left) and A2/NS4B$^+$CD8$^+$ T_{NM}, T_{SCM}, T_{CM}, T_{EM} and T_E cells defined as in **b** (right), normalized to all A2/NS4B$^-$CD8$^+$ T cells. Bold lines, median. Dashed lines, 25th and 75th quartiles; $n = 20$ to 34 donors. Statistics, two-way ANOVA with Šidák's multiple comparisons test (left) and Tukey's multiple comparisons test (right). **d**, Flow cytometry analysis of Ki-67^{hi} cells among all A2/NS4B$^-$ and A2/NS4B$^+$CD8$^+$ T cells (left) or A2/NS4B$^+$CD8$^+$ T_{NM}, T_{SCM}, T_{CM}, T_{EM} and T_E cells defined as in **b** (right). Bold lines, median. Dashed lines, 25th and 75th quartiles; $n = 17$ to 28 donors. norm., normalized. Statistics as in **c**.

activity of A2/NS4B$^+$CD8$^+$ T cells by assessing protein translation, which accounts for approximately half of total cellular ATP consumption[33]. Protein synthesis can be assessed by flow cytometry ex vivo through incorporation of puromycin, which is added to polypeptide chains instead of tyrosyl-tRNA. Differences in puromycin levels between cells treated with translation inhibitor harringtonine and cells without inhibitor defined the basal protein synthesis (BPS) rate. At day 14, A2/NS4B$^+$CD8$^+$ cells exhibited variable BPS rates (Fig. 2b,c), which reflected differences between CD8$^+$ T cell subsets that were not observed in A2/NS4B$^-$CD8$^+$ T cells (Extended Data Fig. 3a). Whereas A2/NS4B$^+$CD8$^+$ T_{NM} cells showed slightly higher BPS than their A2/NS4B$^-$CD8$^+$ counterparts, BPS was highest in A2/NS4B$^+$CD8$^+$ T_{CM} cells (Fig. 2c). By contrast, T_{EM} and T_E cells displayed lower BPS than A2/NS4B$^-$CD8$^+$ cells at day 14 (Fig. 2c). This reflected subpopulations of T_{EM} and T_E cells with low puromycin incorporation (Fig. 2b), consistent with a preapoptotic state. Excluding puro^{lo} subpopulations, A2/NS4B$^+$CD8$^+$ T_{EM} and T_E had mildly elevated BPS at day 14, but T_{CM} cells still had the highest BPS (Extended Data Fig. 3b). Similar results were obtained in 'vaccination-reactive' HLA-DR$^+$CD38$^+$CD8$^+$ cells at day 14 (Extended Data Fig. 3c). In whole blood, BPS was higher in all A2/NS4B$^+$CD8$^+$ cells compared to A2/NS4B$^-$CD8$^+$ cells, and there were no puro^{lo} cells (Extended Data Fig. 3d,e), suggesting that puro^{lo}CD8$^+$ T cells were induced by cryopreservation-associated stress. After day 14, the metabolic activity of A2/NS4B$^+$CD8$^+$ subsets returned to the level of A2/NS4B$^-$CD8$^+$ cells (Fig. 2c and Extended Data Fig. 3f). T_{CM} cells showed the highest level of Ki-67 expression at day 14; this was lower in T_{NM} and in highly differentiated T_E cells (Fig. 2b,d and Extended Data Fig. 3g–i). BPS was higher in Ki-67^{hi} than in Ki-67^{lo} A2/NS4B$^+$CD8$^+$ cells (Extended Data Fig. 3j), confirming a link between metabolic activity and proliferation. Ki-67 was undetectable at 1 year (Fig. 2d and Extended Data Fig. 3k).

To assess whether considering global metabolic activity improved our understanding of T cell subset dynamics, we developed mathematical models to describe T cell proliferation, differentiation and death after YFV vaccination with or without metabolic activity (BPS) as a parameter (Supplementary Figs. 3 and 4). Assuming a linear T_{NM}–T_{SCM}–T_{CM}–T_{EM}–T_E differentiation pathway, we found that including BPS of T cell subsets improved the quantification of cellular dynamics compared to time-constant rates for cell differentiation and turnover[34] or Ki-67 levels (Supplementary Fig. 3a–d). However, additional subset-dependent factors likely influenced cellular turnover (Supplementary Fig. 3e–g). Notably, these models did not exclude the possibility that less differentiated subsets—for instance, T_{NM} cells—may directly differentiate into subsets such as T_{EM} cells. In summary, T_{CM} cells were the most metabolically active subset during the acute phase, and metabolic activity informed differentiation kinetics.

Phenotypic subsets display distinct metabolic programs

Next, we aimed to understand which molecular factors underpinned T cell activation and quiescence. Analysis of published metabolic pathway gene sets (Kyoto Encyclopedia of Genes and Genomes (KEGG), Gene Ontology Biological Process (GOBP), and others) in scRNA-seq data of A2/NS4B$^+$CD8$^+$ T cells on day 14 postvaccination using Vision indicated that pathways associated with ribosomes and quiescence were dominant in T$_{NM}$ cells (Fig. 3a and Supplementary Fig. 5a,b). As high ribosomal gene expression is a hallmark of 'prepared' naive cells[35], this suggested that T$_{NM}$ cells were inactive, yet prepared. Conversely, gene signatures of T cell proliferation, actin cytoskeleton regulation and the proteasome were enriched in the cycling cluster (Fig. 3a and Supplementary Fig. 5b), reflecting high metabolic activity.

Investigation of mean scores for individual pathways among A2/NS4B$^+$CD8$^+$ T cells per time point, transcriptional cluster or CITE-seq phenotype indicated that quiescence was downregulated at day 11–21, when OXPHOS and glycolysis were prominent (Fig. 3b and Supplementary Fig. 5c). Quiescence signatures were most prominent in clusters and CITE-seq populations corresponding to T$_{NM}$ or noncycling T$_{CM}$ cells (Fig. 3b). OXPHOS and glycolysis were both upregulated in cycling cells compared to all other cells (Fig. 3a,b). Cycling cells dominated at day 14 and mainly displayed CD62L$^+$CD45RA$^-$ T$_{CM}$ or CD62L$^-$CD45RA$^-$ T$_{EM}$ CITE-seq phenotypes (Fig. 1h and Supplementary Figs. 2b and 5d). Cycling T$_{CM}$ cells were more active compared to cycling T$_{EM}$ cells and had a pronounced transcriptional OXPHOS signature (Supplementary Fig. 5e,f).

Vision analysis also indicated that apoptosis and base excision repair pathways were both upregulated in cycling cells and followed similar kinetics (Fig. 3b). Apoptosis was upregulated in IFN T$_{EM}$ and IFN T$_E$ clusters (Fig. 3b), indicating contraction in these populations. By contrast, base excision repair was upregulated in the T$_N$/T$_{NM}$ clusters (Fig. 3b), suggesting transcriptional preparedness for genomic surveillance. Linoleic acid metabolism[36] was upregulated from day 28 onward, whereas arachidonic acid signatures[37] were prominent at day 7 and day 365 onward (Supplementary Fig. 5c), revealing time-dependent regulation of understudied metabolic pathways in human antigen-specific T cells. OXPHOS and glycolysis gene scores were increased in A2/NS4B$^+$CD8$^+$ cells compared to A2/NS4B$^-$CD8$^+$ cells in the acute phase but similarly low again in the memory phase (Fig. 3c). OXPHOS gene scores were highest in the cycling cluster, high in T$_N$/T$_{NM}$ clusters and lowest in more differentiated T$_{EM}$ and T$_E$ clusters at day 14 (Fig. 3d,e). The glycolysis score showed similar patterns but was also elevated in noncycling T$_{CM}$ cells at day 14 (Fig. 3d,e). Thus, phenotypic subsets displayed distinct transcriptional metabolic programs during the course of a human T cell response, and, whereas quiescence was associated with stem-like T cells, OXPHOS was most prominent in cycling T$_{CM}$ cells.

T cell activity depends on OXPHOS

Metabolic phenotypes are dynamic and difficult to capture on a transcriptional level. To define metabolic pathway usage in vivo, we analyzed the dependence of protein translation on specific pathways. We used the puromycin-based assay SCENITH (single-cell energetic metabolism by profiling translation inhibition)[38] to measure BPS reduction after inhibiting glycolysis through 2-DG or the mitochondrial ATP-synthase through oligomycin in antigen-specific T cells at day 14 and 1 year after YFV vaccination (Fig. 4a). In the acute phase, glycolytic dependence of A2/NS4B$^+$CD8$^+$ cells (median 13% of BPS) exceeded that of A2/NS4B$^-$CD8$^+$ cells (0%), with T$_{CM}$ cells demonstrating the highest glycolytic dependence (28%) (Fig. 4b and Extended Data Fig. 4a). After 1 year, A2/NS4B$^+$CD8$^+$ cells were no longer dependent on glycolysis (Fig. 4b). In A2/NS4B$^+$CD8$^+$ cells, mitochondrial dependence was higher (47%) than glycolytic dependence at day 14 and reached almost 100% at 1 year (Fig. 4b). Similar dependencies were observed for 'vaccination-reactive' HLA-DR$^+$CD38$^+$ cells, in both cryopreserved and whole-blood samples (Extended Data Fig. 4b,c). MitoTracker Green, indicating mitochondrial mass (Extended Data Fig. 4d), and tetramethylrhodamine methyl ester (TMRM), a marker for mitochondrial membrane potential (Extended Data Fig. 4e), were higher in A2/NS4B$^+$CD8$^+$ T cells compared to A2/NS4B$^-$CD8$^+$ cells at day 14 and 1 year, with the highest mitochondrial activity in T$_{SCM}$ and T$_{CM}$ cells. TMRM reflects absolute mitochondrial activity, whereas SCENITH reports relative dependence. However, TMRM correlated with the relative mitochondrial dependence multiplied by absolute BPS (Extended Data Fig. 4f).

Next, we performed SCENITH on polyclonal CD8$^+$ T cells isolated from blood of healthy donors and activated in vitro with CD3 + CD28 antibodies and IL-2. This indicated that at 24 h, both glycolytic dependence (36%) and BPS were high in T$_{SCM}$ and T$_{CM}$ cells activated in vitro, whereas mitochondrial dependence was highest in T$_N$/T$_{NM}$ cells (Extended Data Fig. 5). However, at 72 h, activated CD8$^+$ T cells showed greater reliance on OXPHOS (40%) compared to glycolysis (3%) (Extended Data Fig. 5), similar to A2/NS4B$^+$CD8$^+$ cells at day 14 post-YFV vaccination. BPS and CD69 and/or CD137 peaked at 24 h, whereas maximum proliferation was detected at 72 h (Extended Data Fig. 5).

To investigate the connection between T cell metabolism and protein translation more mechanistically, we stimulated polyclonal unsorted PBMCs or sorted CD8$^+$ T cell subsets isolated from blood of healthy donors with CD3 + CD28 antibodies and IL-2 for 72 h and treated them with 2-DG (inhibiting glycolysis), oligomycin (inhibiting OXPHOS) or harringtonine (abrogating protein translation) during the first 24 h (Extended Data Figs. 6 and 7). The 2-DG-treated cells showed preferential retention in a CD62L$^+$CD45RA$^+$CD95$^-$ T$_N$/T$_{NM}$ state, whereas oligomycin- and harringtonine-treated cells demonstrated precocious differentiation into CD62L$^-$CD45RA$^+$ T$_E$ cells (Extended Data Fig. 6a–c). Conversely, 2-DG treatment had a milder inhibitory effect on the proliferation of CD8$^+$ T cells, as measured through dilution of CellTrace Far Red or absolute cell counts, compared to oligomycin and harringtonine treatment (Extended Data Fig. 6d–h). CD8$^+$ T cells sorted for a CD62L$^+$CD45RA$^+$CD95$^-$ T$_N$/T$_{NM}$ phenotype

Fig. 3 | CD8$^+$ T cell subsets display distinct transcriptional metabolic programs. a, Vision analysis after scRNA-seq of pathways in A2/NS4B$^+$CD8$^+$ T cells within cycling (left) or *SELL*^{hi} T$_N$/T$_{NM}$ (right) clusters versus all other cells on day 14 post-YFV vaccination and UMAP showing T cell proliferation scores (numbers on UMAP) in the indicated Leiden clusters (*MKI67*^{hi} cycling, *SELL*^{hi} T$_N$/T$_{NM}$, *IL7R*^{hi} T$_{CM}$, *GZMK*^{hi} T$_{EM}$ and *CCL5*^{hi} T$_E$ cells with or without IFN-sensing signature) (middle). Black dots (left and right) indicate pathways with statistically significant log fold change (two-sided *t*-test with Benjamini–Hochberg correction for multiple testing, $P < 0.05$). Gray dots (left and right) indicate nonsignificant pathways. **b**, Transcriptional analysis of A2/NS4B$^+$CD8$^+$ T cell subsets as in **a**, comparing time points postvaccination (left), Leiden cluster localization (middle; defined in **a**) or CITE-seq phenotype (CD62L$^+$CD45RA$^+$CD95$^-$ T$_{NM}$, CD62L$^+$CD45RA$^+$CD95$^+$ T$_{SCM}$, CD62L$^+$CD45RA$^-$ T$_{CM}$, CD62L$^-$CD45RA$^-$ T$_{EM}$, CD62L$^-$CD45RA$^+$ T$_E$ cells; right) and weighted transcript level/pathway (bar graph, right). Pathways with significant enrichment in A2/NS4B$^+$CD8$^+$ compared with A2/NS4B$^-$CD8$^+$ cells are shown (statistics as in **a**). **c**, Transcriptional pathway scores within all A2/NS4B$^+$ and A2/NS4B$^-$ CD8$^+$ T cells at all time points. Bold line, mean. Shaded areas, s.e.m. Statistics, two-way ANOVA with Tukey's multiple comparisons test. **d**, UMAPs with transcriptional pathway scores as in **c** for A2/NS4B$^+$CD8$^+$ T cells at day 14 and 1 year. Colors indicate score per cell. Gray, A2/NS4B$^-$CD8$^+$ T cells. **e**, Transcriptional pathway scores for pathways as in **c** within A2/NS4B$^+$CD8$^+$ T cells grouped by Leiden clusters as in **a** at day 14 and 1 year post-YFV vaccination. Bold lines, median. Dashed lines, 25th and 75th quartiles. Statistics, Kruskal–Wallis test (top, middle) or two-sided Brown–Forsythe and Welch ANOVA tests (bottom). Max., maximum; Min., minimum.

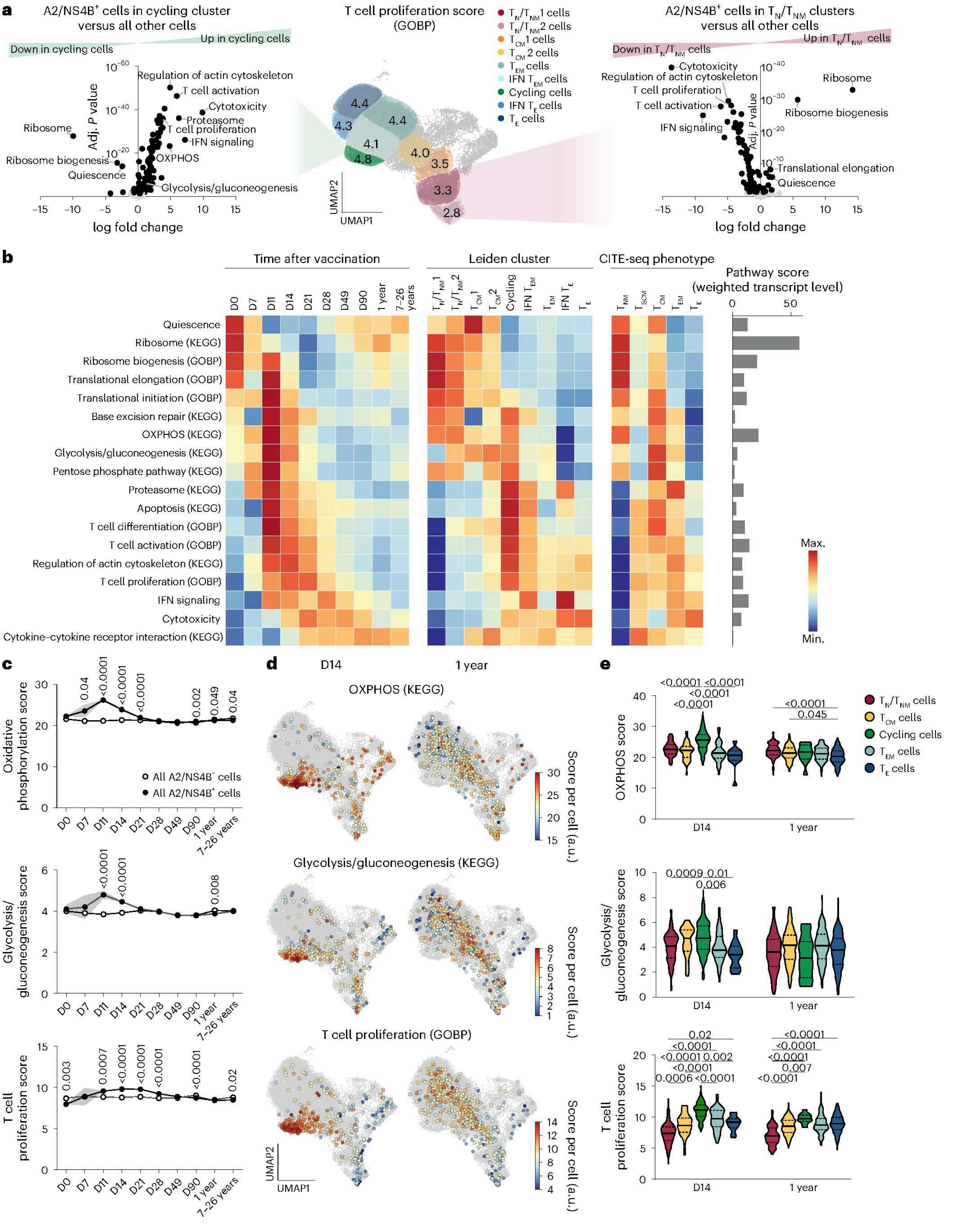
a
A2/NS4B⁺ cells in cycling cluster versus all other cells
Down in cycling cells
Up in cycling cells
Adj. P value
log fold change
Regulation of actin cytoskeleton
T cell activation
Cytotoxicity
Proteasome
T cell proliferation
IFN signaling
OXPHOS
Ribosome
Ribosome biogenesis
Quiescence
Glycolysis/gluconeogenesis
T cell proliferation score (GOBP)
T_N/T_NM1 cells
T_N/T_NM2 cells
T_CM1 cells
T_CM2 cells
T_EM cells
IFN T_EM cells
Cycling cells
IFN T_E cells
T_E cells
4.4
4.3
4.4
4.1
4.8
4.0
3.5
3.3
2.8
UMAP1
UMAP2
A2/NS4B⁺ cells in T_N/T_NM clusters versus all other cells
Down in T_N/T_NM cells
Up in T_N/T_NM cells
Cytotoxicity
Regulation of actin cytoskeleton
T cell proliferation
T cell activation
IFN signaling
Ribosome
Ribosome biogenesis
Translational elongation
Quiescence
b
Time after vaccination
D0 D7 D11 D14 D21 D28 D49 D90 1 year 7–26 years
Leiden cluster
T_N/T_NM1 T_N/T_NM2 T_CM1 T_CM2 Cycling IFN T_EM T_EM IFN T_E T_E
CITE-seq phenotype
T_NM T_SCM T_CM T_EM T_E
Pathway score (weighted transcript level)
0 50
Quiescence
Ribosome (KEGG)
Ribosome biogenesis (GOBP)
Translational elongation (GOBP)
Translational initiation (GOBP)
Base excision repair (KEGG)
OXPHOS (KEGG)
Glycolysis/gluconeogenesis (KEGG)
Pentose phosphate pathway (KEGG)
Proteasome (KEGG)
Apoptosis (KEGG)
T cell differentiation (GOBP)
T cell activation (GOBP)
Regulation of actin cytoskeleton (KEGG)
T cell proliferation (GOBP)
IFN signaling
Cytotoxicity
Cytokine–cytokine receptor interaction (KEGG)
Max.
Min.
c
Oxidative phosphorylation score
0.04 <0.0001 <0.0001 <0.0001 0.002 0.049 0.04
All A2/NS4B⁻ cells
All A2/NS4B⁺ cells
Glycolysis/gluconeogenesis score
<0.0001 <0.0001 0.008
T cell proliferation score
0.003 0.0007 <0.0001 <0.0001 <0.0001 <0.0001 0.02
D0 D7 D11 D14 D21 D28 D49 D90 1 year 7–26 years
d
D14
1 year
OXPHOS (KEGG)
Glycolysis/gluconeogenesis (KEGG)
T cell proliferation (GOBP)
Score per cell (a.u.)
UMAP1
UMAP2
e
OXPHOS score
<0.0001 <0.0001
<0.0001
<0.0001
<0.0001
0.045
Glycolysis/gluconeogenesis score
0.0009 0.01
0.006
T cell proliferation score
0.02
<0.0001
<0.0001 0.002
<0.0001
0.0006 <0.0001
<0.0001
<0.0001
<0.0001
0.007
<0.0001
D14
1 year
T_N/T_NM cells
T_CM cells
Cycling cells
T_EM cells
T_E cells

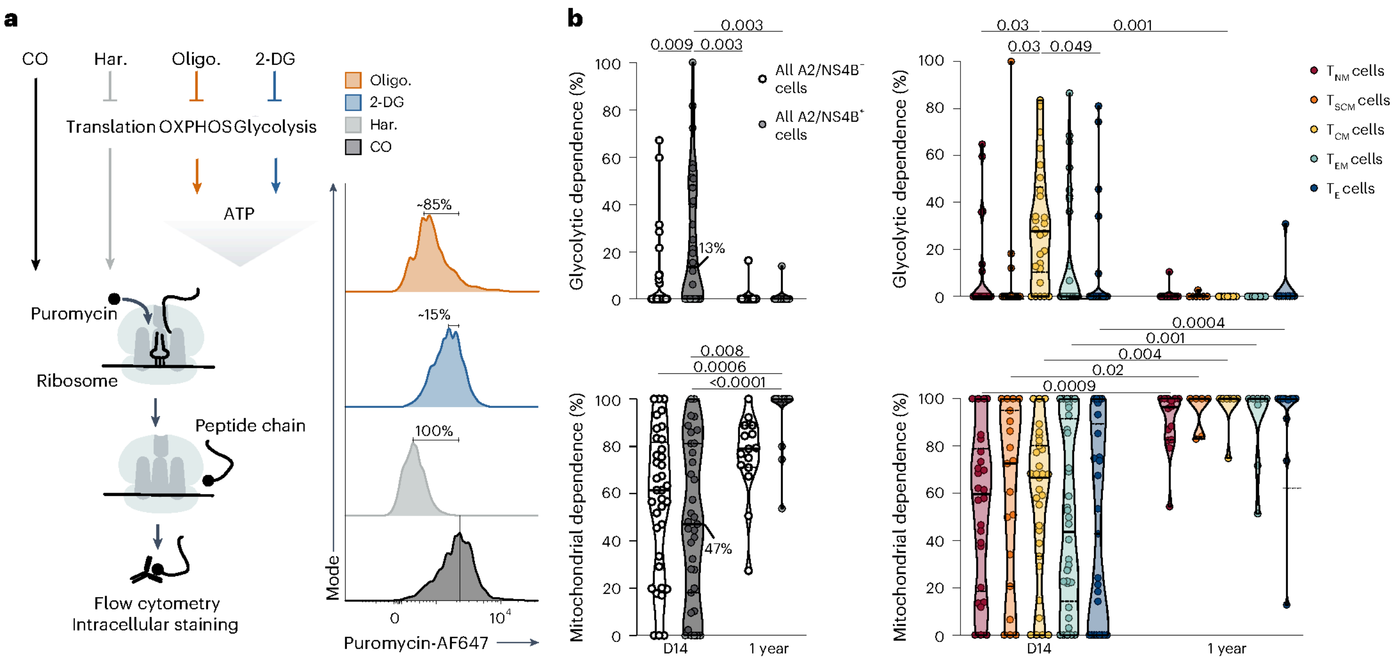

Fig. 4 | CD8$^+$ T cell activity is associated with glycolysis but depends most on OXPHOS. a, Scheme for SCENITH workflow (left) and representative flow cytometry data (right) of A2/NS4B$^+$CD8$^+$ T cells analyzed by SCENITH using DMSO as a control (CO), 2-DG, oligomycin (Oligo.) or harringtonine (Har.). Percentages in the histogram indicate the fraction of protein synthesis lost by inhibitor treatment, with 100% protein synthesis defined as the difference between CO and Har. **b**, Quantification of glycolytic (top) and mitochondrial (bottom) dependence determined as depicted in **a** for all A2/NS4B$^-$CD8$^+$ and A2/NS4B$^+$CD8$^+$ T cells (left) or A2/NS4B$^+$CD8$^+$ T cell subsets (CD62L$^+$CD45RA$^+$CD95$^-$ T_{NM}, CD62L$^+$CD45RA$^+$CD95$^+$ T_{SCM}, CD62L$^+$CD45RA$^-$ T_{CM}, CD62L$^-$CD45RA$^-$ T_{EM} and CD62L$^-$CD45RA$^+$ T_E cells; right). Bold lines, median. Dashed lines, 25th and 75th quartiles. Percentages indicate median metabolic dependencies over all A2/NS4B$^+$CD8$^+$ cells; $n = 14$–34 donors. Statistics, two-way ANOVA with Tukey's multiple comparisons test (left) and Šídák's multiple comparisons test (right).

showed a greater reduction in cell numbers and more pronounced differentiation into CD62L$^-$CD45RA$^+$ T_E cells following oligomycin or harringtonine treatment compared to 2-DG, whereas non-T_N/T_{NM} sorted cells showed diminished upregulation of CD69 and/or CD137 after activation when initially treated with oligomycin or harringtonine (Extended Data Fig. 7). Overall, these results suggest a crucial role for OXPHOS in the maintenance, proliferation and effector function of activated CD8$^+$ T cells.

Quiescence precedes and maintains T cell memory

To explore the molecular basis of quiescence in CD8$^+$ T cells with an early (T_{NM}) or late (T_{EM}/T_E) differentiation stage, we measured cleaved caspase 3 (clCasp-3), a marker of early apoptosis, in antigen-specific cells after YFV vaccination. Cryopreserved A2/NS4B$^+$CD8$^+$ cells expressed high levels of clCasp-3 on day 14, which were not detected in these cells 1 year after vaccination, in A2/NS4B$^-$CD8$^+$ cells on day 14 or in A2/NS4B$^+$CD8$^+$ cells from whole blood (Fig. 5a,b and Extended Data Fig. 8a). Of note, clCasp-3^{hi} A2/NS4B$^+$CD8$^+$ cells were gated on living cells and showed only mildly increased staining with a viability dye, compared to clCasp-3^{lo} A2/NS4B$^+$CD8$^+$ cells (Extended Data Fig. 8b), suggesting that cryopreservation induced apoptotic signaling in epitope-specific cells that were predisposed to apoptosis in vivo. clCasp-3 expression was lowest in T_{NM} cells and highest in more differentiated T_{EM}/T_E A2/NS4B$^+$CD8$^+$ cells at day 14 (Fig. 5a,b), consistent with higher likelihoods of population contraction in these subsets. Similar findings were made in HLA-DR$^+$CD38$^+$ 'vaccination-reactive' cells (Extended Data Fig. 8c,d).

Based on clCasp-3 and puromycin signals, we identified four metabolic subpopulations: puro^{lo}clCasp-3^{lo} metabolically inactive 'healthy quiescent' cells with high prosurvival BCL-2 expression; puro^{hi}clCasp-3^{lo} metabolically active nonapoptotic cells; puro^{hi}clCasp-3^{hi} metabolically active cells transitioning to apoptosis; and puro^{lo}clCasp-3^{hi} 'unhealthy quiescent' cells with reduced BCL-2 expression (Fig. 5c and Extended Data Fig. 8e,f). T_{NM} cells were primarily puro^{lo}clCasp-3^{lo} throughout the entire immune response, similar to A2/NS4B$^-$CD8$^+$ cells (Fig. 5c,d and Extended Data Fig. 8g,h). At day 14, T_{CM} cells were predominantly found in the puro^{hi}clCasp-3^{lo} and puro^{hi}clCasp-3^{hi} subpopulations, whereas the majority of T_{EM} and T_E cells were puro^{lo}clCasp-3^{hi} (Fig. 5c,d). clCasp-3 expression was reduced 1 year postvaccination, when puro^{lo}clCasp-3^{lo} cells dominated in all subsets (Fig. 5c,d and Extended Data Fig. 8g,h). Expression of BCL-2 was reduced in A2/NS4B$^+$CD8$^+$ T_{EM} and T_E cells compared to all A2/NS4B$^-$CD8$^+$ cells at day 14 (Fig. 5e and Extended Data Fig. 8i), suggesting greater predisposition to apoptosis with increased differentiation, whereas retention of high BCL-2 expression in A2/NS4B$^+$CD8$^+$ T_{NM} cells at day 14 confirmed a prosurvival program in these cells (Fig. 5e and Extended Data Fig. 8i). To further differentiate healthy from unhealthy quiescence, we measured γH2AX, a marker of DNA damage and DNA repair during proliferation[39], in the same cells. Preapoptotic A2/NS4B$^+$CD8$^+$ T_{EM} and T_E cells, as well as metabolically active A2/NS4B$^+$CD8$^+$ T_{SCM} and T_{CM} cells, had high expression of γH2AX at day 14, whereas γH2AX expression remained low in T_{NM} cells compared to A2/NS4B$^-$ cells (Fig. 5e and Extended Data Fig. 8i). Expression of γH2AX was also higher in Ki-67^{hi} compared to Ki-67^{lo} A2/NS4B$^+$CD8$^+$ cells (Extended Data Fig. 8j), low in puro^{lo}clCasp-3^{lo} quiescent cells, intermediate in puro^{hi}clCasp-3^{lo} cells and highest in the clCasp-3^{hi} subsets (Extended Data Fig. 8e,f). Thus, T_{NM} cells maintained a healthy quiescent phenotype throughout the immune response, whereas T_{CM} cells, which had the most active metabolism, had weak expression of survival factors and early signs of apoptosis, which were further accentuated in T_{EM} and T_E cells.

T cell subset metabolic activity is conserved across models

To validate our findings in independent model systems, we assessed metabolic signatures in human antigen-specific CD8$^+$ T cells from a SARS-CoV-2 mRNA vaccination cohort using published scRNA-seq data, including blood samples from 13 donors across 7 time points (day 10 after primary, secondary and third vaccination; day 68 to

210 after second vaccination; and day 108 to 189 after third vaccination)[32]. CD8^{+} T cell responses against three immunodominant spike epitopes (HLA-A*01:01/LTD, HLA-A*02:01/YLQ and HLA-A*03:01/KCY) showed similar phenotypic kinetics[32] and were combined for the analysis ('SARS-CoV-2-specific CD8^{+} T cells') (Supplementary Fig. 6a,b). SARS-CoV-2-specific CD8^{+} T cells showed an elevated proliferation pathway score at day 10 after each vaccination and elevated pathway scores for OXPHOS and glycolysis especially at day 10 after primary immunization, but not after subsequent vaccinations (Supplementary Fig. 6c), possibly because transcriptional dynamics are accelerated in recall responses[35]. Upregulated (OXPHOS, proteasome, cytotoxicity) and downregulated (ribosome, quiescence) pathways in antigen-specific cells in the cycling cluster at day 10 after primary SARS-CoV-2 vaccination were highly comparable with those observed in the cycling cluster at day 14 post-YFV vaccination (Supplementary Fig. 6d).

We next performed SCENITH-based analysis of metabolic pathway dependence in the same cohort[32], focusing on A2/YLQ pHLA tetramer-binding CD8^{+} T cells on day 10 after second immunization (Extended Data Fig. 9a,b). Fifty-seven percent of A2/YLQ^{+}CD8^{+} T cells were CD62L^{-}CD45RA^{-} T$_{\mathrm{EM}}$ cells (Extended Data Fig. 9c,d). Whereas A2/YLQ^{+}CD62L^{+}CD45RA^{-} T$_{\mathrm{CM}}$ cells exhibited the highest BPS, T$_{\mathrm{EM}}$ cells were less metabolically active than the average A2/YLQ^{-}CD8^{+} T cell population, which resulted in the total A2/YLQ^{+}CD8^{+} T cell population appearing less active (Extended Data Fig. 9e,f). Moreover, A2/YLQ^{+}CD8^{+} T cells showed greater dependence of protein translation on OXPHOS compared to glycolysis (Extended Data Fig. 9g), and clCasp-3 expression was correlated with T cell differentiation (Extended Data Fig. 9h–j). Overall, SARS-CoV-2 mRNA vaccination induced fewer CD8^{+} T$_{\mathrm{NM}}$ or T$_{\mathrm{E}}$ cells than YFV vaccination, but the metabolic qualities of the subsets that were more robustly induced, T$_{\mathrm{CM}}$ and T$_{\mathrm{EM}}$, were conserved across immunization settings.

In mouse models of bacterial and viral infection, we conducted SCENITH analyses of transferred OT-I or P14 T cells (which are specific for OVA epitope SIINFEKL or gp$_{33-41}$ epitope KAVYNFATC) isolated from the blood of recipient C57BL/6 wild-type mice at day 6, 8, 10, and 30 to 35 after infection with OVA-expressing *Listeria monocytogenes* or lymphocytic choriomeningitis virus (LCMV) Armstrong, respectively (Extended Data Fig. 10a). Intermediate-differentiated CD27^{+}CD62L^{+}KLRG1^{+} T$_{\mathrm{CM}}$ and CD27^{+}CD62L^{-} T$_{\mathrm{EM}}$ cells had the highest BPS, whereas least-differentiated CD27^{+}CD62L^{+}KLRG1^{-} T$_{\mathrm{CM}}$ cells were less active at day 6 (acute phase), with endogenous CD27^{+}CD62L^{+}KLRG1^{-} T$_{\mathrm{CM}}$ cells as baseline in both models (Extended Data Fig. 10b,c). Mouse CD8^{+} T cells strongly relied on glycolysis (median >40 %) throughout the immune response (Extended Data Fig. 10d,e). Thus, CD8^{+} T cell subset-dependent metabolic activity levels were similar between humans and mice, whereas mouse CD8^{+} T cells were more reliant on glycolysis compared to human CD8^{+} T cells.

Discussion

We assessed protein translation to measure the metabolic activity and pathway dependence of human antigen-specific CD8^{+} T cells after in vivo immunization. After YFV vaccination, human T$_{\mathrm{NM}}$ cells were healthy quiescent and formed the dominant population of memory CD8^{+} T cells. T$_{\mathrm{CM}}$ cells were the metabolically most active subset, and T$_{\mathrm{EM}}$ and T$_{\mathrm{E}}$ cells were unhealthy quiescent, characterized by low protein translation and induction of clCasp-3. All CD8^{+} T cells depended primarily on OXPHOS throughout the immune response.

Comparison of in vivo models of immunization in humans and mice showed consistent associations between differentiation and metabolic activity but differences in the abundance of T cell subsets and dependencies on specific metabolic pathways. Mouse KLRG1^{-} T$_{\mathrm{CM}}$ corresponded to human T$_{\mathrm{NM}}$ cells, compatible with the observation that mouse KLRG1^{-} T$_{\mathrm{CM}}$ cells proliferate little but feed recall responses[8]. In SARS-CoV-2-vaccinated humans, epitope-specific T$_{\mathrm{NM}}$ cells were less abundant than T$_{\mathrm{CM}}$ and T$_{\mathrm{EM}}$ cells, which precluded assessment of metabolic activity in T$_{\mathrm{NM}}$ cells. The metabolic characteristics of SARS-CoV-2- and YFV-specific T$_{\mathrm{CM}}$ and T$_{\mathrm{EM}}$ cells were similar.

The idea that activated T cells are glycolytic and resting T cells are dependent on OXPHOS has been challenged in recent years. Mouse T cells analyzed ex vivo already engage OXPHOS during the acute phase and use glycolysis during the acute and memory phase for anabolic needs and to control reactive oxygen species[40–42]. Our study shows the importance of OXPHOS for energy production in all phenotypic T cell subsets, at acute and memory time points in humans and mice. Glycolysis, by contrast, was upregulated only in the acute phase in human T cells and was detected mainly in the most proliferative subset (T$_{\mathrm{CM}}$). Thus, human antigen-specific T cells activated in vivo relied primarily on OXPHOS for catabolism, whereas the association of increased metabolic activity and dependence on glycolysis in T$_{\mathrm{CM}}$ cells suggested a role for anabolism in this T cell subset. This was consistent with reports that human or mouse T cells rely on glycolysis to switch on cytokine-producing effector functions[18,43] and that T$_{\mathrm{EM}}$ cells possess reduced mitochondrial metabolic profiles compared to T$_{\mathrm{CM}}$ cells[24,44]. With advances in single-cell metabolomics[45], future work could identify the precise metabolic network associated with the transient glycolytic burst—for example, the pentose phosphate or hexosamine pathway—that generates the molecular building blocks of proliferating cells[46].

We detected subpopulations of T$_{\mathrm{EM}}$ and T$_{\mathrm{E}}$ cells with reduced metabolic activity (puro$^{\mathrm{lo}}$) and a predisposition for apoptosis, as well as puro$^{\mathrm{hi}}$ T$_{\mathrm{EM}}$ and T$_{\mathrm{E}}$ cells. More differentiated T cells have shorter half-lives in vivo[47,48] but can be maintained long-term[10–12]. However, interventional studies in mouse models suggest that little-divided quiescent cells with an early-differentiated (CD62L^{+}TCF-1^{+}) phenotype and resilience toward replicative stress persist longest and drive recall responses[8,13,34,39]. In accordance with those studies, we found that human antigen-specific T$_{\mathrm{NM}}$ cells already stopped initial mild proliferative and metabolic activity at day 11–14 postvaccination without a need for DNA damage responses[49]. Considering T$_{\mathrm{NM}}$ survival decades after YFV vaccination, this provides experimental evidence for a link between metabolic quiescence and immunological memory formation in humans.

Fig. 5 | Metabolic quiescence precedes and maintains CD8^{+} T cell memory. **a**, Representative flow cytometry histograms of clCasp-3 expression in all A2/NS4B^{-}CD8^{+} cells, all A2/NS4B^{+}CD8^{+} cells and A2/NS4B^{+}CD8^{+} T cell subsets (CD62L^{+}CD45RA^{+}CD95^{-} T$_{\mathrm{NM}}$, CD62L^{+}CD45RA^{+}CD95^{+} T$_{\mathrm{SCM}}$, CD62L^{+}CD45RA^{-} T$_{\mathrm{CM}}$, CD62L^{-}CD45RA^{-} T$_{\mathrm{EM}}$, CD62L^{-}CD45RA^{+} T$_{\mathrm{E}}$ cells) in whole blood (left) and cryopreserved samples (right) on day 14 post-YFV vaccination. **b**, clCasp-3$^{\mathrm{hi}}$ cells in all A2/NS4B^{-}CD8^{+} and all A2/NS4B^{+}CD8^{+} cells (left) or A2/NS4B^{+}CD8^{+} T$_{\mathrm{NM}}$, T$_{\mathrm{SCM}}$, T$_{\mathrm{CM}}$, T$_{\mathrm{EM}}$ and T$_{\mathrm{E}}$ cells defined as in **a** (right) for cryopreserved samples post-YFV vaccination by flow cytometry. Bold lines, median. Dashed lines, 25th and 75th quartiles. $n = 16$–33 donors. Statistics, two-way ANOVA with Šídák's multiple comparisons test (left) and Tukey's multiple comparisons test (right). **c**,**d**, Representative flow cytometry plots (**c**) and quantification of puro$^{\mathrm{lo}}$clCasp-3$^{\mathrm{lo}}$, puro$^{\mathrm{hi}}$clCasp-3$^{\mathrm{lo}}$, puro$^{\mathrm{hi}}$clCasp-3$^{\mathrm{hi}}$ and puro$^{\mathrm{lo}}$clCasp-3$^{\mathrm{hi}}$ subpopulations (**d**) in cryopreserved A2/NS4B^{+}CD8^{+} cells (all cells) and A2/NS4B^{+}CD8^{+} T$_{\mathrm{NM}}$, T$_{\mathrm{SCM}}$, T$_{\mathrm{CM}}$, T$_{\mathrm{EM}}$ and T$_{\mathrm{E}}$ cells defined as in **a** (at day 14 and 1 year post-YFV vaccination in **c**, and at day 7 to 1 year postvaccination in **d**). Lines indicate the mean and shaded areas the s.e.m. Statistically significant changes over time by two-way ANOVA (puro$^{\mathrm{lo}}$clCasp-3$^{\mathrm{lo}}$ cells among all A2/NS4B^{+}CD8^{+}, T$_{\mathrm{CM}}$, T$_{\mathrm{EM}}$, T$_{\mathrm{E}}$ cells; puro$^{\mathrm{hi}}$clCasp-3$^{\mathrm{lo}}$ cells among T$_{\mathrm{SCM}}$, T$_{\mathrm{CM}}$, T$_{\mathrm{EM}}$ cells; puro$^{\mathrm{hi}}$clCasp-3$^{\mathrm{hi}}$ cells among all A2/NS4B^{+}CD8^{+}, T$_{\mathrm{CM}}$, T$_{\mathrm{EM}}$ cells; and puro$^{\mathrm{lo}}$clCasp-3$^{\mathrm{hi}}$ cells among A2/NS4B^{+}CD8^{+}, T$_{\mathrm{EM}}$, T$_{\mathrm{E}}$ cells), with Tukey's multiple comparisons test (each subset tested against A2/NS4B^{+}CD8^{+} T cells) shown in **d**; $n = 4$ to 38 donors. **e**, BCL-2 (left) and yH2AX (right) MFI in cryopreserved A2/NS4B^{-} or A2/NS4B^{+}CD8^{+} T$_{\mathrm{NM}}$, T$_{\mathrm{SCM}}$, T$_{\mathrm{CM}}$, T$_{\mathrm{EM}}$ and T$_{\mathrm{E}}$ cells defined as in **a** at day 14 post-YFV vaccination analyzed by flow cytometry, normalized to A2/NS4B^{-}CD8^{+} T cells. Bold lines, median. Dashed lines, 25th and 75th quartiles. $n = 11$ (left) and $n = 13$ (right) donors. Statistics, Kruskal–Wallis test with Dunn's multiple comparisons test (each subset against A2/NS4B^{-}CD8^{+} T cells).

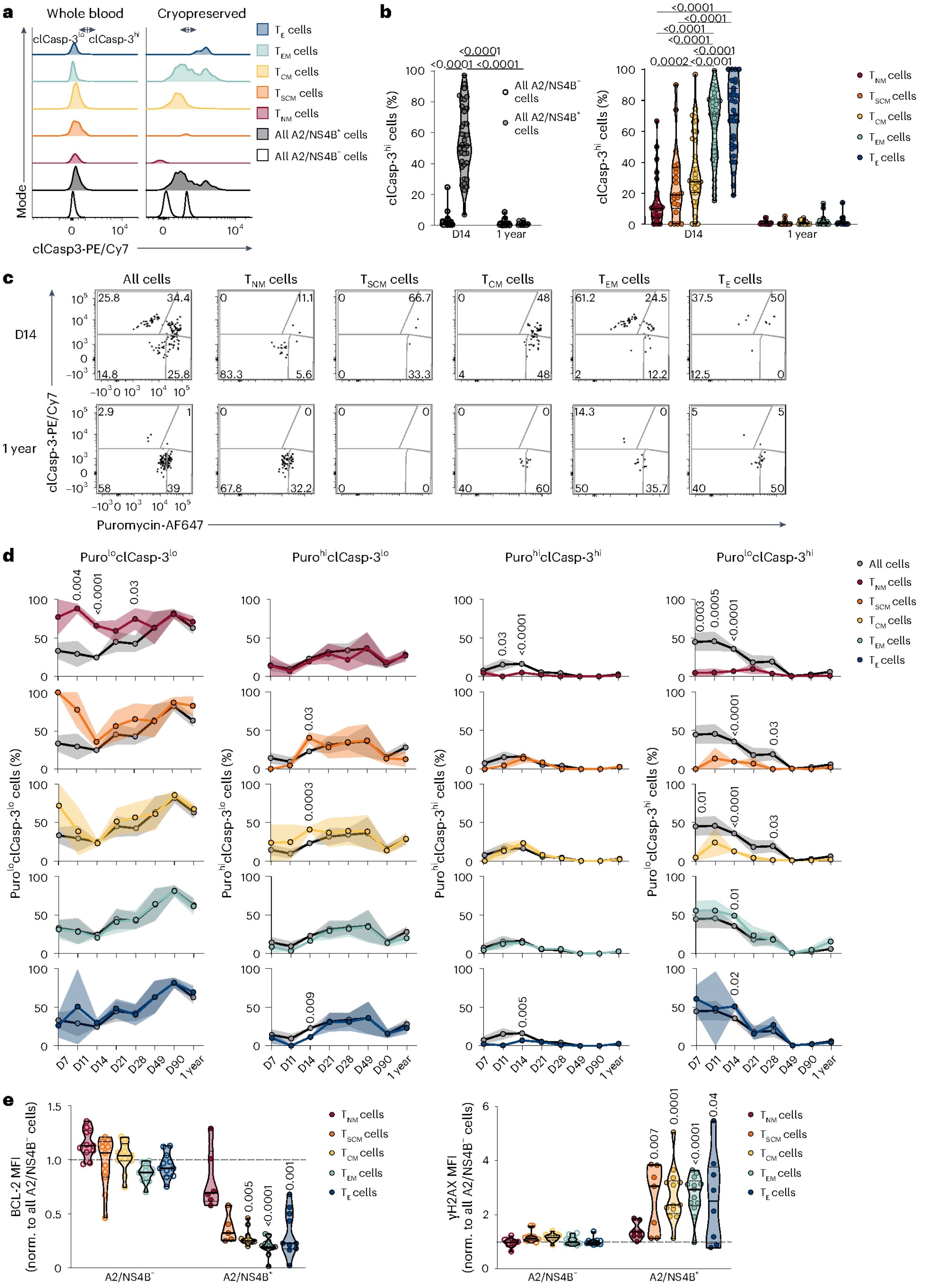
a
Whole blood
Cryopreserved
clCasp-3lo clCasp-3hi
Mode
0
10⁴
clCasp3-PE/Cy7
TE cells
TEM cells
TCM cells
TSCM cells
TNM cells
All A2/NS4B+ cells
All A2/NS4B− cells
b
clCasp-3hi cells (%)
<0.0001
<0.0001 <0.0001
D14
1 year
All A2/NS4B− cells
All A2/NS4B+ cells
<0.0001
<0.0001
<0.0001
<0.0001
<0.0001
0.0002 <0.0001
TNM cells
TSCM cells
TCM cells
TEM cells
TE cells
c
All cells
TNM cells
TSCM cells
TCM cells
TEM cells
TE cells
D14
1 year
clCasp-3-PE/Cy7
Puromycin-AF647
25.8 34.4 14.8 25.8
0 11.1 83.3 5.6
0 66.7 0 33.3
0 48 4 48
61.2 24.5 2 12.2
37.5 50 12.5 0
2.9 1 58 39
0 0 67.8 32.2
0 0 0 0
0 0 40 60
14.3 0 50 35.7
5 5 40 50
−10³ 0 10³ 10⁴ 10⁵
d
Purolo clCasp-3lo
Purohi clCasp-3lo
Purohi clCasp-3hi
Purolo clCasp-3hi
Purolo clCasp-3lo cells (%)
Purohi clCasp-3lo cells (%)
Purohi clCasp-3hi cells (%)
Purolo clCasp-3hi cells (%)
0.004
<0.0001
0.03
0.03
0.0003
0.009
0.03
<0.0001
0.005
0.003
0.0005
<0.0001
<0.0001
0.03
0.01
<0.0001
0.03
0.01
0.02
D7 D11 D14 D21 D28 D49 D90 1 year
All cells
TNM cells
TSCM cells
TCM cells
TEM cells
TE cells
e
BCL-2 MFI (norm. to all A2/NS4B− cells)
A2/NS4B−
A2/NS4B+
0.005
<0.0001
0.001
γH2AX MFI (norm. to all A2/NS4B− cells)
0.007
0.0001
<0.0001
0.04
TNM cells
TSCM cells
TCM cells
TEM cells
TE cells

Online content

Any methods, additional references, Nature Portfolio reporting summaries, source data, extended data, supplementary information, acknowledgements, peer review information; details of author contributions and competing interests; and statements of data and code availability are available at https://doi.org/10.1038/s41590-026-02421-w.

References

1. Fuertes Marraco, S. A. et al. Long-lasting stem cell–like memory CD8$^+$ T cells with a naïve-like profile upon yellow fever vaccination. *Sci. Transl. Med.* **7**, 282ra48 (2015).
2. Adamo, S. et al. Memory profiles distinguish cross-reactive and virus-specific T cell immunity to mpox. *Cell Host Microbe* **9**, 223–238 (2023).
3. Akondy, R. S. et al. Origin and differentiation of human memory CD8 T cells after vaccination. *Nature* **552**, 362–367 (2017).
4. Adamo, S. et al. Signature of long-lived memory CD8$^+$ T cells in acute SARS-CoV-2 infection. *Nature* **602**, 148–155 (2022).
5. Müller, T. R. et al. Additive effects of booster mRNA vaccination and SARS-CoV-2 Omicron infection on T cell immunity across immunocompromised states. *Sci. Transl. Med.* **15**, eadg9452 (2023).
6. Busch, D. H., Fräßle, S. P., Sommermeyer, D., Buchholz, V. R. & Riddell, S. R. Role of memory T cell subsets for adoptive immunotherapy. *Semin. Immunol.* **28**, 28–34 (2016).
7. Gattinoni, L., Speiser, D. E., Lichterfeld, M. & Bonini, C. T memory stem cells in health and disease. *Nat. Med.* **23**, 18–27 (2017).
8. Bresser, K. et al. Replicative history marks transcriptional and functional disparity in the CD8$^+$ T cell memory pool. *Nat. Immunol.* **23**, 791–801 (2022).
9. Graef, P. et al. Serial transfer of single-cell-derived immunocompetence reveals stemness of CD8$^+$ central memory T cells. *Immunity* **41**, 116–126 (2014).
10. Kaech, S. M., Hemby, S., Kersh, E. & Ahmed, R. Molecular and functional profiling of memory CD8 T cell differentiation. *Cell* **111**, 837–851 (2002).
11. Garrod, K. R. et al. Dissecting T cell contraction in vivo using a genetically encoded reporter of apoptosis. *Cell Rep.* **2**, 1438–1447 (2012).
12. Dolfi, D. V. et al. Late signals from CD27 prevent Fas-dependent apoptosis of primary CD8$^+$ T cells. *J. Immunol.* **180**, 2912–2921 (2008).
13. Kretschmer, L. et al. Differential expansion of T central memory precursor and effector subsets is regulated by division speed. *Nat. Commun.* **11**, 113 (2020).
14. Chapman, N. M., Boothby, M. R. & Chi, H. Metabolic coordination of T cell quiescence and activation. *Nat. Rev. Immunol.* **20**, 55–70 (2020).
15. Reina-Campos, M., Scharping, N. E. & Goldrath, A. W. CD8$^+$ T cell metabolism in infection and cancer. *Nat. Rev. Immunol.* **21**, 718–738 (2021).
16. Roos, D. & Loos, J. A. Changes in the carbohydrate metabolism of mitogenically stimulated human peripheral lymphocytes. II. Relative importance of glycolysis and oxidative phosphorylation on phytohaemagglutinin stimulation. *Exp. Cell. Res.* **77**, 127–135 (1973).
17. Pearce, E. L. et al. Enhancing CD8 T-cell memory by modulating fatty acid metabolism. *Nature* **460**, 103–107 (2009).
18. Chang, C.-H. et al. Posttranscriptional control of T cell effector function by aerobic glycolysis. *Cell* **153**, 1239–1251 (2013).
19. van der Windt, G. J. W. et al. Mitochondrial respiratory capacity is a critical regulator of CD8$^+$ T cell memory development. *Immunity* **36**, 68–78 (2012).
20. Ma, E. H. et al. Metabolic profiling using stable isotope tracing reveals distinct patterns of glucose utilization by physiologically activated CD8$^+$ T cells. *Immunity* **51**, 856–870 (2019).
21. Frisch, A. T. et al. Redirecting glucose flux during in vitro expansion generates epigenetically and metabolically superior T cells for cancer immunotherapy. *Cell Metab.* **37**, 870–885 (2025).
22. Liikanen, I. et al. Hypoxia-inducible factor activity promotes antitumor effector function and tissue residency by CD8$^+$ T cells. *J. Clin. Invest.* **131**, e143729 (2021).
23. Sukumar, M. et al. Inhibiting glycolytic metabolism enhances CD8$^+$ T cell memory and antitumor function. *J. Clin. Invest.* **123**, 4479–4488 (2013).
24. Phan, A. T. et al. Constitutive glycolytic metabolism supports CD8$^+$ T cell effector memory differentiation during viral infection. *Immunity* **45**, 1024–1037 (2016).
25. Pulendran, B., Oh, J. Z., Nakaya, H. I., Ravindran, R. & Kazmin, D. A. Immunity to viruses: learning from successful human vaccines. *Immunol. Rev.* **255**, 243–255 (2013).
26. Theiler, M. & Smith, H. H. The effect of prolonged cultivation in vitro upon the pathogenicity of yellow fever virus. *J. Exp. Med.* **65**, 767–786 (1937).
27. Niedrig, M., Lademann, M., Emmerich, P. & Lafrenz, M. Assessment of IgG antibodies against yellow fever virus after vaccination with 17D by different assays: neutralization test, haemagglutination inhibition test, immunofluorescence assay and ELISA. *Trop. Med. Int. Heal.* **4**, 867–871 (1999).
28. Akondy, R. S. et al. The yellow fever virus vaccine induces a broad and polyfunctional human memory CD8$^+$ T cell response. *J. Immunol.* **183**, 7919–7930 (2009).
29. Stryhn, A. et al. A systematic, unbiased mapping of CD8$^+$ and CD4$^+$ T cell epitopes in yellow fever vaccinees. *Front. Immunol.* **11**, 1836 (2020).
30. Gattinoni, L. et al. A human memory T cell subset with stem cell-like properties. *Nat. Med.* **17**, 1290–1297 (2011).
31. Cossarizza, A. et al. Guidelines for the use of flow cytometry and cell sorting in immunological studies (second edition). *Eur. J. Immunol.* **49**, 1457–1973 (2019).
32. Kocher, K. et al. Vaccination-induced T cell responses maintain polyclonality with high antigen receptor avidity. *Sci. Immunol.* **10**, 1–19 (2025).
33. Schmidt, E. K., Clavarino, G., Ceppi, M. & Pierre, P. SUnSET, a nonradioactive method to monitor protein synthesis. *Nat. Methods* **6**, 275–277 (2009).
34. Buchholz, V. R. et al. Disparate individual fates compose robust CD8$^+$ T cell immunity. *Science* **340**, 630–635 (2013).
35. Wolf, T. et al. Dynamics in protein translation sustaining T cell preparedness. *Nat. Immunol.* **21**, 927–937 (2020).
36. Nava Lauson, C. B. et al. Linoleic acid potentiates CD8$^+$ T cell metabolic fitness and antitumor immunity. *Cell Metab.* **35**, 633–650 (2023).
37. Bibby, J. A. et al. Systematic single-cell pathway analysis to characterize early T cell activation. *Cell Rep.* **41**, 111697 (2022).
38. Argüello, R. J. et al. SCENITH: a flow cytometry-based method to functionally profile energy metabolism with single-cell resolution. *Cell Metab.* **32**, 1063–1075 (2020).
39. Johnnidis, J. B. et al. Inhibitory signaling sustains a distinct early memory CD8$^+$ T cell precursor that is resistant to DNA damage. *Sci. Immunol.* **6**, eabe3702 (2021).
40. van der Windt, G. J. W. & Pearce, E. L. Metabolic switching and fuel choice during T-cell differentiation and memory development. *Immunol. Rev.* **249**, 27–42 (2012).
41. Zhang, H. et al. TCR activation directly stimulates PYGB-dependent glycogenolysis to fuel the early recall response in CD8$^+$ memory T cells. *Mol. Cell* **82**, 3077–3088 (2022).
42. Ma, R. et al. A Pck1-directed glycogen metabolic program regulates formation and maintenance of memory CD8$^+$ T cells. *Nat. Cell Biol.* **20**, 21–27 (2018).

43. Gubser, P. M. et al. Rapid effector function of memory CD8$^+$ T cells requires an immediate-early glycolytic switch. *Nat. Immunol.* **14**, 1064–1072 (2013).
44. Nicoli, F. et al. Naïve CD8$^+$ T-cells engage a versatile metabolic program upon activation in humans and differ energetically from memory CD8$^+$ T-cells. *Front. Immunol.* **9**, 2736 (2018).
45. Artyomov, M. N. & Van den Bossche, J. Immunometabolism in the single-cell era. *Cell Metab.* **32**, 710–725 (2020).
46. O'Neill, L. A. J., Kishton, R. J. & Rathmell, J. A guide to immunometabolism for immunologists. *Nat. Rev. Immunol.* **16**, 553–565 (2016).
47. Kaech, S. M. et al. Selective expression of the interleukin 7 receptor identifies effector CD8 T cells that give rise to long-lived memory cells. *Nat. Immunol.* **4**, 1191–1198 (2003).
48. Lugli, E. et al. Superior T memory stem cell persistence supports long-lived T cell memory. *J. Clin. Invest.* **123**, 594–599 (2013).
49. Araki, K. et al. Translation is actively regulated during the differentiation of CD8$^+$ effector T cells. *Nat. Immunol.* **18**, 1046–1057 (2017).

---

[1]Mikrobiologisches Institut–Klinische Mikrobiologie, Immunologie und Hygiene, Universitätsklinikum Erlangen, Friedrich-Alexander-Universität Erlangen-Nürnberg, Erlangen, Germany. [2]Department of Internal Medicine 5 - Hematology and Oncology, Friedrich-Alexander-Universität Erlangen-Nürnberg (FAU) and Universitätsklinikum Erlangen, Erlangen, Germany. [3]Biological Information Processing Group, BioQuant, Heidelberg University, Heidelberg, Germany. [4]Institute for Medical Microbiology, Immunology, and Hygiene, School of Medicine and Health, Technical University of Munich, Munich, Germany. [5]Deutsches Zentrum Immuntherapie, FAU Erlangen-Nürnberg and Universitätsklinikum Erlangen, Erlangen, Germany. [6]Division of Functional Immune Cell Modulation, Leibniz Institute for Immunotherapy, Regensburg, Germany. [7]University of Regensburg, Regensburg, Germany. [8]Center for Immunomedicine in Transplantation and Oncology, University Hospital Regensburg, Regensburg, Germany. [9]Division of Immunology, German Cancer Research Center (DKFZ), Heidelberg, Germany. [10]Institute of Computational Biology, Helmholtz Zentrum München — German Research Center for Environmental Health, Neuherberg, Germany. [11]Institute of Clinical Pharmacology, LMU University Hospital, LMU Munich, Munich, Germany. [12]Einheit für Klinische Pharmakologie (EKLiP), Helmholtz Zentrum München German Research Center for Environmental Health (HMGU), Neuherberg, Germany. [13]German Center for Infection Research, Partner Site Munich, Munich, Germany. [14]FAU Profile Center Immunomedicine, FAU Erlangen-Nürnberg, Erlangen, Germany. [15]These authors contributed equally: Sina Frischholz, Ev-Marie Schuster, Myriam Grotz. ✉e-mail: kilian.schober@uk-erlangen.de

Methods

Ethics regulations

Ethics approval for the yellow fever study (number 350_20 B; clinical trial ID: DRKS00034356) was granted by the local ethics committee (Medical Faculty, University Hospital Erlangen, Friedrich-Alexander University Erlangen-Nürnberg, Germany). Samples were collected after written consent had been provided by the donors, and donors received financial compensation. Additional cryopreserved peripheral blood mononuclear cells (PBMCs) from 22 donors vaccinated with the YFV-17D vaccine were provided by S. Rothenfusser (LMU Munich). Approval for this cohort was granted by the review board of the Medical Faculty of LMU (number 86-16), and cohort details are described in the ISRCTN registry (17974967). Animal experiments were approved by the district government of upper Bavaria (Department 5: Environment, Health and Consumer Protection).

Study cohorts

Yellow fever vaccination donors ($n = 76$) were 20–62 years old (median: 26; interquartile range: 23–31 years), 62% female, of European Caucasian ethnicity, overall healthy (no chronic medication), of normal weight, and received the YFV-17D vaccine (Supplementary Table 1). No previous YFV vaccination or yellow fever infection was reported for any donor. Thirty-one donors had received other vaccinations (rabies, typhoid, meningococcal disease, tetanus/diphtheria/pertussis/polio, cholera, hepatitis A, hepatitis B, rick-borne encephalitis, Japanese encephalitis, COVID-19) between day −14 before and day 13 after vaccination. Nine donors vaccinated with the SARS-CoV-2 mRNA vaccine Comirnaty were included from the previously described CoVa-Adapt cohort[32], with blood collected from all donors on day 10 after the second vaccination. HLA typing was conducted at the University Hospital of Erlangen (Supplementary Table 6). PBMCs were isolated from citrated peripheral blood by density-gradient centrifugation using Bio-Coll density medium (BioSell, BS.L 6115). Cells were analyzed directly in fresh whole blood or cryopreserved in fetal calf serum (FCS) + 10% dimethyl sulfoxide (DMSO) in liquid nitrogen.

Multimerization of pHLA monomers

Biotinylated HLA-A*02:01 molecules loaded with LLWNGPMAV peptide (yellow fever NS4B$_{214-222}$) or YLQPRTFLL peptide (SARS-CoV-2 spike protein) were generated[50] and multimerized on a streptavidin backbone conjugated with PE-fluorophores (Life Technologies, 12-4317-87) or BV421-fluorophores (BioLegend, 405225). Per 1×10^6 cells, 0.2 µg pHLA was mixed with 0.125 µg streptavidin-PE or 0.05 µg streptavidin-BV421 in 25 µL FACS buffer (phosphate-buffered saline (PBS) + 0.5% bovine serum albumin) for 30 min (4 °C) directly before staining.

Flow cytometry

The following antibodies were used for human samples: anti-CD3-BUV496 (741206; 1:100), anti-CD4-PE/CF594 (562316; 1:200), anti-CD4-BV786 (740962; 1:400), anti-CD8-BUV395 (563795; 1:200), anti-CD8-BUV496 (612942; 1:200), anti-CD19-PE/CF594 (562294; 1:200), anti-CD56-PE/CF594 (564963; 1:200), anti-HLA-DR-BV421 (562805; 1:400), anti-HLA-DR-APC (560744; 1:200), anti-CD38-BV605 (562666; 1:400), anti-CD38-BUV395 (563812; 1:200), anti-CD95-BUV737 (612790; 1:20), anti-CD95-BV421 (566258; 1:25), anti-Ki-67-BV711 (563755; 1:20), anti-CD69-PE/Cy7 (561928; 1:100) anti-BCL-2-PE (556535; 1:100), anti-yH2AX-PE (562377; 1:20) and anti-HLA-A2-FITC (551285; 1:100) from BD Biosciences; anti-CD8-APC (301049; 1:200), anti-CD4-BV510 (300545; 1:50), anti-CD62L-FITC (304804; 1:200), anti-CD62L-APC/Cy7 (304813; 1:100), anti-CCR7-FITC (353215; 1:100), anti-mouse TCR β chain-APC/Fire 750 (109246; 1:100) and anti-CD45RA-PerCP/Cy5.5 (304121; 1:400) from BioLegend; anti-CD4-PE (12-0049-42; 1:400), anti-CD8-eF450 (48-0086-42; 1:200), anti-CD56-FITC (11-0566-42; 1:200), anti-CD45-PerCP/Cy5.5 (45-0459-42; 1:100) and anti-CD45-PE/Cy7 (25-9459-42; 1:400) from eBioScience; anti-puromycin-AF647 (MABE343-AF647; 1:200), anti-puromycin-AF488 (MABE343-AF488; 1:200) from Sigma-Aldrich; anti-CD8-FITC (A07756; 1:200) from Beckman Coulter; anti-CD45-PB (PB986, 1:50) from DAKO; anti-CD137-PE (130-119-885; 1:100) from Miltenyi; and anti-clCasp-3-PE/Cy7 (64772S; 1:50) from Cell Signaling Technology. A ZombieAqua or Zombie NIR Fixable Viability Kit (BioLegend; 4231017/423102; 1:500) was used for viability staining.

For murine samples, the antibodies were anti-puromycin-AF647 (MABE343-AF647; 1:200) from Sigma-Aldrich; anti-CD45.1-FITC (110706; 1:100), anti-KLRG1-PE/Cy7 (138416; 1:100), anti-CD27-mCherry (124228; 1:100), anti-CD4-APC/Cy7 (100414; 1:300), anti-CD8-BV785 (100750; 1:200), anti-CD19-APC/Cy7 (115530; 1:300) from BioLegend; and anti-CD62L-BUV737 (612833; 1:200) from BD Biosciences. Viability staining was performed using Fixable Viability Dye eFluor-780 (Thermo Fisher, 65-0865-18; 1:1,000).

Staining was performed at 4 °C. PBMCs or murine cells were washed with FACS buffer. When required, cells ($1–2 \times 10^6$) were incubated with pHLA multimers (25 µl) for 25 min, followed by addition of 25 µl FACS buffer containing surface antibodies and viability stain with further incubation for 20 min. Samples without pHLA multimers were stained identically, except that the multimer incubation was omitted. For intracellular staining, cells were fixed and permeabilized using a BD Cytofix/Cytoperm Kit (BD Biosciences, 554714) for human samples or an eBioscience Foxp3/Transcription Factor Staining Buffer Set (Invitrogen by Thermo Fisher Scientific, 00-5523-00) for murine samples, then incubated for 60 min with intracellular antibodies in PermWash (50 µl per 1×10^6 cells). Cells were analyzed using a LSRFortessa Cell Analyzer (BD Biosciences) with FlowJo v.10.7.2 (Tree Star Inc.). Unless indicated otherwise, we gated on single, living CD19$^-$CD56$^-$CD4$^-$CD3$^+$CD8$^+$ A2/NS4B$^+$ or A2/NS4B$^-$ cells.

Metabolic profiling of cryopreserved PBMCs ex vivo

The SCENITH protocol was adapted from Argüello et al.[38]. Cryopreserved PBMCs were rested overnight (37 °C; 5% CO_2) in cRPMI$^-$ (RPMI 1640 Medium (Life Technologies; 21875091), 10% heat-inactivated FCS (anprotec; AC-SM-0027), 0.05 mM β-mercaptoethanol (Life Technologies; 31350010), 1.1915 g l^{-1} HEPES (Carl Roth; HN77.3), 0.2 g l^{-1} L-glutamine (Fisher Scientific; 31870025)). For analysis at day 0–49 after vaccination, 1×10^6 PBMCs (1×10^6 cells ml^{-1} in cRPMI$^-$) were plated into a 24-well plate. For 1-year samples or SARS-CoV-2 samples, 2×10^6 PBMCs per well were plated in a 12-well plate. Cells were rested for 1 h (37 °C; 5% CO_2). Metabolic inhibitors were prepared in PBS to reach the required final concentration: 2-DG (100 mM; Sigma-Aldrich; D6134), oligomycin (1 µM; Sigma-Aldrich; 75351), and harringtonine (2 µg ml^{-1}; Santa Cruz Biotechnology; sc-204771); controls received an equal volume of DMSO in PBS. Cells were treated for 15 min with inhibitors (37 °C; 5% CO_2), followed by addition of puromycin (10 µg µl^{-1}; Sigma-Aldrich; P7255) for 25 min (37 °C; 5% CO2). Cells were washed with FACS buffer, stained for extracellular markers, and stained intracellularly for puromycin and additional markers. BPS and metabolic dependencies were calculated from the geometric mean fluorescence intensity (MFI) of puromycin:

$$\mathrm{BPS} = \mathrm{MFI}_{\mathrm{puromycin}}[\mathrm{CO} - \mathrm{Har.}]$$

$$\text{Glycolytic dependence} = 100 \times \mathrm{MFI}_{\mathrm{puromycin}} \frac{[\mathrm{CO} - \text{2-DG}]}{[\mathrm{CO} - \mathrm{Har.}]}$$

$$\text{Mitochondrial dependence} = 100 \times \mathrm{MFI}_{\mathrm{puromycin}} \frac{[\mathrm{CO} - \mathrm{Oligo.}]}{[\mathrm{CO} - \mathrm{Har.}]},$$

where CO represents the control, Har. is harringtonine and Oligo. is oligomycin. For metabolic dependencies <0 or >100, the value was set to 0 or 100, respectively.

Metabolic profiling of in vitro stimulated cryopreserved PBMCs

Cryopreserved PBMCs were rested overnight in cRPMI$^-$ (37 °C, 5% CO_2). Then, 0.25×10^6 cells (1×10^6 cells ml^{-1} in cRPMI$^-$) per well were activated in a 96-well F-bottomed plate with plate-bound anti-CD3 (1 µg ml^{-1}; BioLegend, 317302) and anti-CD28 (1 µg ml^{-1}; BioLegend, 302902) for 24, 48 or 72 h (37 °C, 5% CO_2). Metabolic profiling was performed directly in the 96-well F-bottomed plate using SCENITH as described above. Afterward, staining was performed in a 96-well V-bottomed plate as described above.

Metabolic profiling in whole blood ex vivo

First, 5 µl metabolic inhibitor or control was added to 100 µl freshly drawn whole blood to final concentrations of 100 mM 2-DG, 1 µM oligomycin and 2 µg ml^{-1} harringtonine for 15 min (37 °C, 100 rpm). Puromycin (15 µg ml^{-1}) was then added for 25 min, followed by washing with PBS and surface staining for 20 min (4 °C, 100 rpm). The required volume of surface antibodies and viability dye was prepared to achieve the indicated final concentration in blood samples (without FACS buffer). Erythrocytes were lysed with FACS lysing solution (BD BioScience; 349202), and cells were permeabilized, stained and analyzed as described for cryopreserved PBMCs.

Metabolic profiling of murine cells

Female C57BL/6 mice (CD45.1$^-$, 6–8 weeks old) were purchased from Inotiv. OT-I or P14 donor mice (CD45.1$^+$) were bred under specific-pathogen-free conditions at the mouse facility of Technische Universität München. Mice were fed a T.2018SMI.12 Global 18% Protein Rodent Diet.

Naive (CD44^{lo}) CD8$^+$ T cells were sorted from the peripheral blood of OT-I or P14 donor mice on a FACS Aria II (Becton Dickinson), and 50,000 (OT-I) or 100,000 (P14) cells were injected intraperitoneally into C57BL/6 recipients. One day after transfer, recipient mice were infected by injecting 5×10^3 colony-forming units of recombinant OVA-expressing *L. monocytogenes* (LM) intravenously or 2×10^5 plaque-forming units of LCMV Armstrong intraperitoneally. Blood was sampled on days 6 and 835 (first LM-OVA experiment) or days 0, 6, 8, 10 and 30 (second LM-OVA and LCMV Armstrong experiments) after infection. Lysis was performed with Ammonium chloride-Tris (90% (v/v) 0.17 M NH_4Cl, 10% (v/v) 0.17 M Tris HCl, pH 7.2). Cells were plated in a 48-well plate at approximately $0.3–0.5 \times 10^6$ cells (1×10^6 cells ml^{-1} in cRPMI$^-$) per well. Cells were rested for 1 h (37 °C, 5% CO_2) and then SCENITH-treated as cryopreserved PBMCs ex vivo.

Metabolic tracker analysis

Freshly isolated PBMCs (1×10^6 ml^{-1}) were incubated in cRPMI$^-$ containing TMRM (0.05 µM; VWR, T5428-25mg) or MitoTracker Green (1:100; Life Technologies, M46750) for 30 min (37 °C, 5% CO_2), stained with pHLA multimers and surface antibodies (as described) and analyzed on an LSRFortessa Cell Analyzer.

Proliferation of CD8$^+$ T cell subsets under metabolic perturbation

Cryopreserved PBMCs of healthy donors were rested overnight (37 °C, 5% CO_2) in cRPMI$^+$ (cRPMI$^-$ plus 0.05 mg ml^{-1} gentamicin (Life Technologies; 15750060) and 100 U ml^{-1} penicillin–streptomycin (Life Technologies; 15140122)). Cells were washed, resuspended in PBS (1×10^6 cells ml^{-1}) and labeled with CellTrace Far Red (0.5 µM; Thermo Fisher; C34572) for 20 min (37 °C, dark). Cells were washed, resuspended in cRPMI$^+$ and rested for 30 min (37 °C, 5% CO_2). Then, 0.25×10^6 cells per well were stimulated in a 96-well F-bottomed plate with plate-bound anti-CD3 and anti-CD28 (37 °C, 5% CO_2), 50 U ml^{-1} IL-2 for up to 72 h. Where indicated, metabolic inhibitors were added for the first 24 h (10 mM 2-DG, 0.05 µM oligomycin or 0.1 µg ml^{-1} harringtonine). Counting beads (123count eBeads; Life Technologies; 01-1234-42) were added to each well 0 h, 24 h, 48 h and 72 h after stimulation. Cells were transferred to a V-bottomed 96-well plate, washed with FACS buffer, and stained for extracellular markers and analyzed as described. For quantification of cell counts, we normalized the acquired cell numbers to counting beads for each sample.

Analysis of sorted CD8$^+$ T cell subsets under metabolic perturbation

Cryopreserved PBMCs were rested overnight in cRPMI$^+$ (37 °C, 5% CO_2) and washed with FACS buffer, and CD8$^+$ T cells were enriched by magnetic cell separation (MACS; Miltenyi Biotec; 130-096-495): 250×10^6 cells were resuspended in 1 ml of MACS separation buffer (MACS buffer); 250 µl biotin–antibody cocktail was added for 5 min (4 °C), and 750 µl of MACS buffer and 500 µL CD8$^+$ MicroBeads were added for 10 min (4 °C). Cells were separated according to the manufacturer's instructions.

CD8$^+$ T cells were stained with surface antibodies (CD62L, CD45RA, CD8, CD95) and sorted on a MoFlo Astrios EQ (Beckman Coulter) into CD8$^+$ input populations: T_N/T_{NM} (CD45RA$^+$CD62L$^+$CD95$^-$) input 1); T_{SCM} (CD45RA$^+$CD62L$^+$CD95$^+$) plus T_{CM} (CD45RA$^-$CD62L$^+$) (input 2); and T_{EM} (CD45RA$^-$CD62L$^-$) plus T_E (CD45RA$^+$CD62L$^-$) (input 3). Cells were washed, resuspended in cRPMI$^+$ and rested for 1 h (37 °C, 5% CO_2).

Next, 0.2×10^6 cells per well were stimulated in a 96-well F-bottomed plate with plate-bound anti-CD3 and anti-CD28 and 50 U ml^{-1} IL-2 (37 °C, 5% CO_2). Where indicated, cells were treated for the first 24 h of stimulation with metabolic inhibitors: 10 mM 2-DG, 0.05 µM oligomycin or 0.1 µg ml^{-1} harringtonine. Before stimulation (0 h sample) or 72 h after stimulation, counting beads were added to each well. Cells were transferred to a V-bottomed 96-well plate, washed with FACS buffer, stained for flow cytometry (as described), fixed using a BD Cytofix Kit and acquired with a Cytek NorthernLights instrument. Cells were pregated on living lymphocytes. For quantification of cell counts, we normalized the acquired cell numbers to counting beads for each sample.

TCR reexpression in Jurkat cells

Six TCRs identified in scRNA-seq were reexpressed in Jurkat TCR-null cells[51]. The TCR constructs contained the identified variable regions of the α and β chains and murine constant regions (Supplementary Table 7). RD114 cells (in cDMEM$^-$ (DMEM (Life Technologies, 11995073) with 10% heat-inactivated FCS, 0.05 mM β-mercaptoethanol, 1.1915 g l^{-1} HEPES and 0.2 g l^{-1} L-glutamine)) were transfected at 60–80% confluence with Lipofectamine 3000 transfection reagent (Thermo Fisher, L3000015) and 2 µg of plasmid DNA according to the manufacturer's instructions. Cells were rested for 6 h (37 °C, 5% CO_2) and medium was replaced with cDMEM$^+$ (cDMEM$^-$ with 0.05 mg ml^{-1} gentamicin and 100 U ml^{-1} penicillin–streptomycin). Viral supernatant was collected after 48 h and stored at 4 °C. For transduction, 700 µl viral supernatant with 8 µg ml^{-1} Polybrene was combined with 0.2×10^6 Jurkat TCR-null cells in 200 µl cRPMI$^+$, plated in a 24-well plate, centrifuged for 2 h (2,000*g*; 32 °C) and incubated for 48 h (37 °C, 5% CO_2) before virus was removed. Cells were cultured for another 48 h in cRPMI$^+$ (with 50 U ml^{-1} IL-2; 37 °C, 5% CO_2). Transduction efficiency and TCR specificity were evaluated by staining mTRBC and A2/NS4B-pHLA multimer (as described).

Single-cell RNA sequencing

scRNA-seq was performed on PBMCs from 18 donors across 9 time points after vaccination and PBMCs from 3 vaccination-naive and 5 long-term vaccinated donors preenriched for antigen-specific cells (Supplementary Table 6). Cryopreserved PBMCs were rested overnight (1×10^6 cells ml^{-1} in cRPMI$^-$). Antigen-specific T cells were detected using PE- and DNA-barcoded MHC-I dCODE dextramers (Immudex) targeting eight YFV epitopes, alongside control dextramers for common viral antigens (Supplementary Table 3). Surface protein expression was assessed using CITE-seq antibodies.

Experiments 1 and 2 included time points spanning day 7 to 26 years. Dextramer cocktails were prepared directly before cell staining (all YFV and control virus dextramers regardless of HLA compatibility for experiment 1; only HLA-A2/NS4B$_{214-222}$ dextramer for experiment 2 (Supplementary Table 6)). Per 5 × 10^6 cells, 1 µl of each dextramer and 0.2 µl of D-biotin (100 µM per dextramer) were combined in 50 µl FACS buffer. PBMCs from different donors were color- and DNA-barcoded using anti-CD45 fluorophore combinations (anti-CD45-PacificBlue, anti-CD45-PerCP/Cy5.5, anti-CD45-PE/Cy7) and TotalSeq-C hashtag antibodies (2.5 µl per 5 × 10^6 PBMCs of TotalSeq-C anti-human hashtag antibodies 1–8; BioLegend: 394661, 394663, 394665, 394667, 394669, 394671, 394673, 394675). Cells were stained for 30 min (4 °C) and washed with FACS buffer, and up to 8 samples with different CD45 and hashtag antibodies were combined. Pooled samples (40–60 × 10^6 cells) were stained with preprepared dextramer pools (50 µl per 5 × 10^6 cells) for 30 min (4 °C). Surface antibodies and viability dye (anti-CD19-PE/CF594, anti-CD56-FITC, anti-CD8-APC, anti-CD4-BV510, Zombie NIR) and CITE-seq TotalSeq-C antibodies (per 5 × 10^6 cells: 0.078 µg anti-human-CD45RA (304163), 0.078 µg anti-human-CD62L (304851), 0.3125 µg anti-human-CD95 (305651), 0.277 µg anti-human-CCR7 (353251), 0.25 µg anti-human-CXCR3 (353251); BioLegend) were added for 30 min (4 °C). Single, living CD19$^-$CD56$^-$CD4$^-$CD8$^+$dextramer$^+$ lymphocytes were sorted on a BD FACS Aria II cell sorter into FCS-coated 1.5-ml tubes containing FACS buffer. In addition, single, living CD19$^-$CD56$^-$CD4$^-$CD8$^+$ lymphocytes irrespective of dextramer signal were added to the sample to provide a general map of CD8$^+$ T cells. The donors were distinguished during sorting by CD45 color barcoding to avoid overrepresentation of individual donors.

In experiment 3, samples from YFV-naive or long-term-vaccinated donors were used. Only the HLA-A2/NS4B$_{214-222}$ dextramer was used, and this was prepared directly before cell staining (as described). PBMCs (10 × 10^6 per donor) were collected, stained with dextramer (100 µl) for 30 min (4 °C) and washed with FACS buffer. Dextramer-specific cells were enriched by MACS (Miltenyi Biotec) with anti-PE microbeads according to the manufacturer's instructions. Enriched cells were stained with surface, CD45 and CITE-seq antibodies and sorted (as described).

Sorted cells were loaded onto a Chromium Next GEM Chip K (10x Genomics) and Chromium Next GEM Single-Cell 5′ Kits (v.2) to generate gene expression (GEX), TCR (VDJ) and cell surface libraries (10x Genomics; 1000263, 1000256, 1000252, 1000286, 1000250, 1000215, 1000190). Libraries were sequenced at Novogene (Cambridge, UK) on an Illumina NovaSeq platform with the PE150 strategy.

scRNA-seq data analysis

The dataset comprised results from three experiments, run across nine sequencing lanes. Processing was performed per lane using Cell Ranger Multi (cellranger-7.1.0, 10x Genomics) with GRCh38 for gene expression (v. 2020A, 10x Genomics), vdj-GRCh38 for VDJ (v. 5.0.0, 10x Genomics) and custom feature barcode references for surface antibody detection.

Single-cell analyses were performed using Scanpy (v.1.10.1)[52] and Scirpy (v.0.14.0)[53]. For each sequencing run, the gene expression and antibody capture matrices were merged with TCR contig annotations, and filtering for doublets and dying cells was applied, based on UMI counts, detected genes and mitochondrial fractions (Supplementary Table 8).

Gene expression data were normalized to 10,000 counts per cell and log1p-transformed. Donor and time point assignments were performed with HashSolo[54]. Samples were integrated, batch-corrected using combat, and cells without annotated TCRs were excluded. Analysis was based on the top 5,000 highly variable genes (excluding TCR genes). UMAP[55] embeddings were computed using 15 neighbors, and Leiden clustering[56] was performed at a resolution of 1. Differential gene expression was assessed using a *t*-test with Benjamini–Hochberg correction via the scanpy.tl.rank_genes_groups function.

Diffusion pseudotime was determined by scanpy.tl.dpt (root cell in cluster 4). Surface protein expression data were transformed using centered log-ratio normalization. Virtual gating was based on centered log-ratio-transformed values for CD45RA, CD62L and CD95, with thresholds of 1.3, 1.6 and 1.0, respectively.

Clonotypes were defined as having identical α- and β-CDR3 amino acid sequences on either the primary or secondary chain. Clonal expansion was assessed across the dataset. For experiment 1, a bivariate Gaussian distribution was used via the sklearn package (v.1.5.0)[57] to distinguish dextramer binding and nonbinding cells based on UMI counts and cell purity (proportion of epitope-specific UMIs among total UMIs). In experiments 2 and 3, cells were stained only with the HLA-A2/NS4B$_{214-222}$ dextramer, so purity metrics were unavailable. Instead, an in-house prediction package was established and applied (Supplementary Methods). A clone was considered to be epitope-specific if >60% of its cells were predicted to be epitope-specific in HLA-matched donors.

Visionpy (v.0.2.0)[58] (https://github.com/YosefLab/visionpy) was used for pathway analysis. Pathway annotations for KEGG legacy and GOBP were obtained from MSigDB (https://www.gsea-msigdb.org/gsea/msigdb) were supplemented with manually curated pathways (Supplementary Table 9). Weighted transcript levels were calculated using Visionpy[58]. Scanpy (scanpy.tl.rank_genes_groups) was used to identify differentially active pathways between clusters. For visualization, mean scores per condition were *z*-scored. Transcription factor network activities were assessed using a univariate linear model on the 'collectri' library in Decoupler (v.1.8.0)[59].

Microarray gene expression data for different T cell subsets (T$_N$, T$_{SCM}$, T$_{CM}$ and T$_{EM}$) from Gattinoni et al.[30] (GEO: GSE23321) were processed in R (v.4.5.1). The CEL files were imported and normalized with oligo (v.1.72.0) using array-specific package pd.hugene.1.0.st.v1 (v.3.14.1). Probes were annotated using hugene10sttranscriptcluster.db (v.8.8.0) and AnnotationDbi (v.1.70.0). Unmapped probes and duplicate genes were removed with dyplr (v.1.1.4), and the resulting expression matrix was used to determine differentially expressed genes in Python (v.3.13.5) with statsmodels (v.0.14.5). From this information, gmt files for the various subsets were generated for investigation using visionpy.

CITE-seq marker analysis

To determine which markers had the greatest potential to identify T$_N$/T$_{NM}$ cells, we analyzed a previously published dataset[32] containing CD8$^+$ T cells stained with 130 CITE-seq antibodies. The T$_N$/T$_{NM}$ Leiden cluster was identified based on marker genes, and the cells were annotated as naive. For each CITE-seq marker, we then determined the optimal signal cutoff for identification of naive cells by calculating positive and negative predictive values for each marker.

Statistics and reproducibility

No statistical methods were used to predetermine sample sizes, but our sample sizes were based on results from previous publications[1,3,28]. The study was nonrandomized, and all consenting donors were included and analyzed. No blinding was performed, as the purpose of the study was not to perform a comparison between different donors but to provide methodological proof-of-concept in multiple donors. Samples were pseudonymized using study identification numbers. We excluded T cell subsets with fewer than ten cells from downstream analyses (exact donor numbers per panel are described in Supplementary Table 2).

Data analysis and visualization

Data graphs were generated with GraphPad Prism 10. Data were tested for normal distribution, then the appropriate statistical test was chosen. In all graphs, only statistically significant results are highlighted. For statistical testing of the timelines in Fig. 5d and Extended Data Fig. 8h, we used two-way analysis of variance with Tukey's multiple comparison post hoc test, although the dataset contains samples from the same donor taken at different time points across the timeline and from donors taken at an individual time point. The test was performed for one subset against all A2/NS4B$^+$CD8$^+$ cells as indicated in the graph. Schemes and figures were generated with Affinity Designer (Serif (Europe) Ltd, v. 2.5.3).

Reporting summary

Further information on research design is available in the Nature Portfolio Reporting Summary linked to this article.

Data availability

All single-cell sequencing data that were newly generated for this study are publicly available on NCBI GEO with accession code GSE298237. Source data are provided with this paper.

Code availability

The source code to analyze the sequencing data is available via GitHub at https://github.com/SchoberLab/YF_scRNAseq.

References

50. Busch, D. H., Pilip, I. & Pamer, E. G. Evolution of a complex T cell receptor repertoire during primary and recall bacterial infection. *J. Exp. Med.* **188**, 61–70 (1998).
51. Müller, T. R. et al. A T-cell reporter platform for high-throughput and reliable investigation of TCR function and biology. *Clin. Transl. Immunol.* **9**, e1216 (2020).
52. Wolf, F. A., Angerer, P. & Theis, F. J. SCANPY: large-scale single-cell gene expression data analysis. *Genome Biol.* **19**, 15 (2018).
53. Sturm, G. et al. Scirpy: a Scanpy extension for analyzing single-cell T-cell receptor-sequencing data. *Bioinformatics* **36**, 4817–4818 (2020).
54. Bernstein, N. J. et al. Solo: doublet identification in single-cell RNA-seq via semi-supervised deep learning. *Cell Syst.* **11**, 95–101 (2020).
55. McInnes, L., Healy, J., Saul, N. & Großberger, L. UMAP: uniform manifold approximation and projection. *J. Open Source Softw.* **3**, 861 (2018).
56. Traag, V. A., Waltman, L. & van Eck, N. J. From Louvain to Leiden: guaranteeing well-connected communities. *Sci. Rep.* **9**, 5233 (2019).
57. Pedregosa, F. et al. Scikit-learn: machine learning in Python. *J. Mach. Learn. Res.* **12**, 2825–2830 (2011).
58. DeTomaso, D. et al. Functional interpretation of single cell similarity maps. *Nat. Commun.* **10**, 4376 (2019).
59. Badia-I-Mompel, P. et al. decoupleR: ensemble of computational methods to infer biological activities from omics data. *Bioinform. Adv.* **2**, vbac016 (2022).

Acknowledgements

This work was supported by grants from the BMFTR (German Federal Ministry of Research, Technology and Space, projects 01KI2013 and 031L0290B), the Else Kröner-Fresenius-Stiftung (project 2020_EKEA.127) and the German Research Foundation (DFG) through research training group (RTG) 2504 (project 401821119) to K.S.; the Yellow4FLAVI project (grant agreement no. 101137459) to S.R. and K.S. and the SCIMAP project (grant agreement no. 949719) to V.R.B funded by the European Union under the Horizon Europe Programme; the BMFTR (project 031L0290A) to B. Schubert; the Boehringer Ingelheim Foundation within the Rise up! program (project RETENTION) and the Hightech Agenda Bavaria to F.G.; the Klaus Tschira Stiftung (project 00.013.2019) to J.P.; FlavImmunity, a combined grant of the DFG (project 391217598) and the French National Research Agency (ANR) (project ANR-17-CE15-0031-01) to S.R.; the DFG TRR237 grant (project 369799452) to S.R. (TPB14); and grants of the iMed consortium of the German Helmholtz Societies to S.R. C.B. was supported by the DFG (grant BO996/7-1 and the RTG 2740 'Immunomicrotope', project 447268119). The study was funded by the European Union. Views and opinions expressed are those of the authors only and do not necessarily reflect those of the European Union or European Health and Digital Executive Agency (HaDEA). The funders had no role in study design, data collection and analysis, decision to publish or preparation of the manuscript. We thank all study participants for making this work possible. We also thank members of the Schober laboratory for experimental support and critical discussion; C. Moosmann and M. Sousa of the Microbiology Institut, University Hospital Erlangen, for graphical and experimental help, respectively; and M. Väth of the Institute of Systems Immunology, Julius-Maximilians University of Würzburg, for critical discussion. Finally, we acknowledge the support of the Manfred Roth-Stiftung, Fürth, Germany, and thank the Core Unit Cell Sorting and Immunomonitoring Erlangen.

Author contributions

Conceptualization: K.S.; data curation: S.F., E.-M.S. and M.G.; formal analysis: S.F., E.-M.S., M.G., S.V. and F.D.; funding acquisition: K.S. and S.R.; investigation: S.F., E.-M.S., M.G., L.K., C.S., J.B., T.H., S.V. and B. Spriewald; methodology: S.F., E.-M.S., M.G., S.V., T.H., K.K., B. Spriewald and F.G.; project administration: K.S.; resources: J.H., R.A., J.E., J.T., V.R.B., L.G., S.R., B. Schubert, D.H.B., C.B. and K.S.; software: M.G., F.G., J.P. and B. Schubert; supervision: K.S., E.-M.S., F.G., J.P. and V.R.B., validation: S.F., E.-M.S. and M.G.; visualization: S.F., E.-M.S. and K.S.; writing—original draft: K.S., E.-M.S. and S.F.; writing—review and editing: all authors.

Funding

Open access funding provided by Friedrich-Alexander-Universität Erlangen-Nürnberg.

Competing interests

The authors declare no competing interests.

Additional information

Extended data is available for this paper at https://doi.org/10.1038/s41590-026-02421-w.

Supplementary information The online version contains supplementary material available at https://doi.org/10.1038/s41590-026-02421-w.

Correspondence and requests for materials should be addressed to Kilian Schober.

Peer review information *Nature Immunology* thanks the anonymous reviewers for their contribution to the peer review of this work. Peer reviewer reports are available. Primary Handling Editor: Ioana Staicu, in collaboration with the *Nature Immunology* team.

Reprints and permissions information is available at www.nature.com/reprints.

https://doi.org/10.1038/s41590-026-02421-w

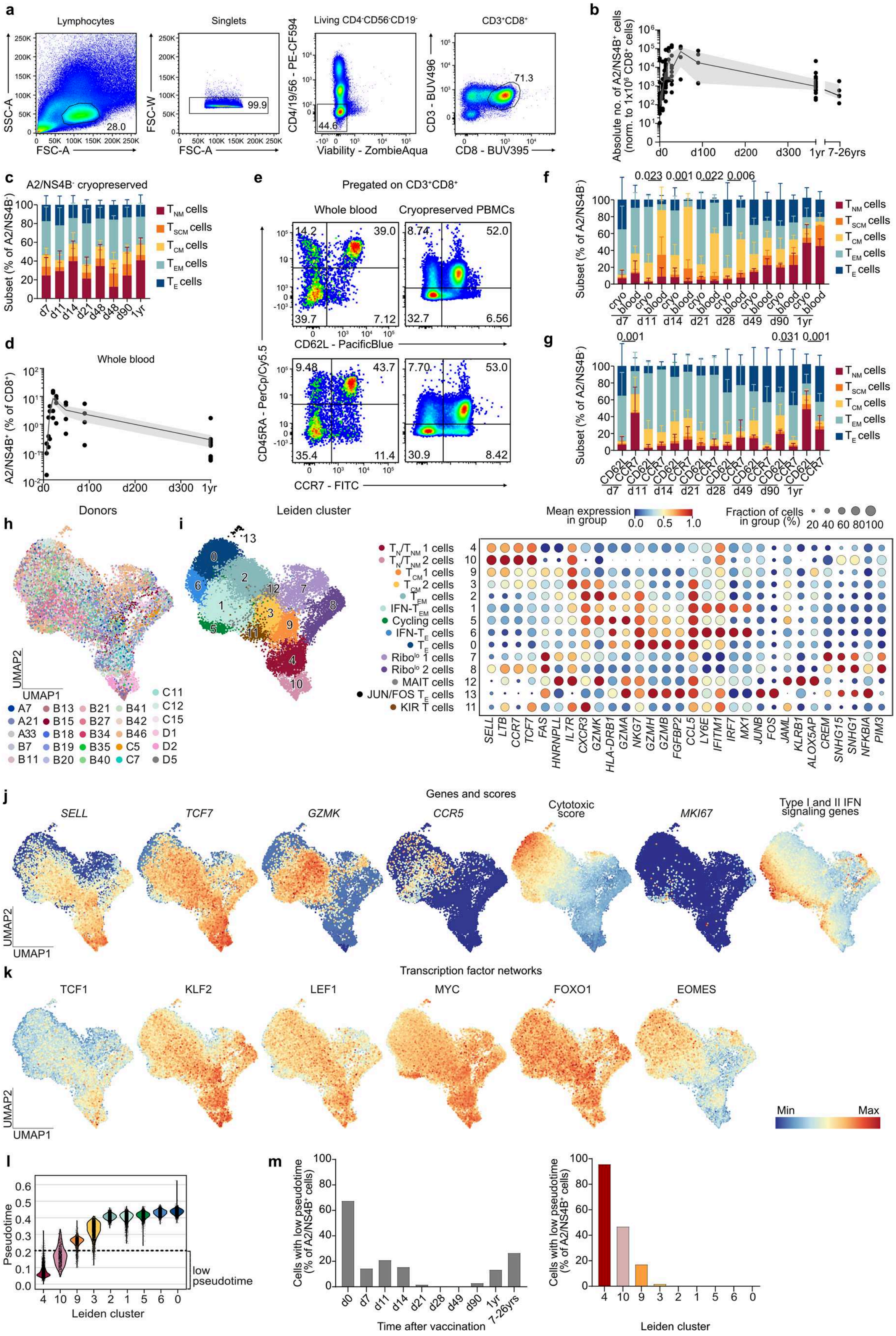

Extended Data Fig. 1 | See next page for caption.

Extended Data Fig. 1 | YFV-specific CD8$^+$ T cells undergo phenotypic dynamics. **a**, Representative flow cytometry gating strategy. **b**, Absolute numbers of A2/NS4B$^+$CD8$^+$ T cells post-YFV vaccination by flow cytometry, normalized to 1×10^6 CD8$^+$ T cells. Solid line, median. Gray area, 25th and 75th confidence interval. n = 4-38 donors. **c**, A2/NS4B$^-$CD8$^+$ T cell subsets (CD62L$^+$CD45RA$^+$CD95$^-$ T_{NM}, CD62L$^+$CD45RA$^+$CD95$^+$ T_{SCM}, CD62L$^+$CD45RA$^-$ T_{CM}, CD62L$^-$CD45RA$^-$ T_{EM}, CD62L$^-$CD45RA$^+$ T_E cells) post-YFV vaccination by flow cytometry. Bars, mean and SEM n = 4-38 donors. Statistics, two-sided permanova comparing subset composition at all timepoints (8 groups, 999 permutations, p-value 0.111). **d**, A2/NS4B$^+$CD8$^+$ T cells after vaccination in whole blood by flow cytometry. Data points, individual donors. Solid line, mean. Gray area, SD **e**, Representative flow cytometry plots of CD8$^+$ T cells stained with CD62L or CCR7 in whole blood or cryopreserved samples. **f**, A2/NS4B$^+$CD8$^+$ T cell subsets (defined in c) after vaccination in cryopreserved cells and whole blood by flow cytometry. Bars, mean and SEM. n = 3-38 (cryo) and n = 3-12 (blood) donors. Statistics, two-sided permanova within each day (2 groups, 999 permutations). **g**, A2/NS4B$^+$CD8$^+$ T cell subsets (defined in c) using CD62L or CCR7 instead of CD62L in flow cytometry. Bars, mean and SEM. n = 3-38 (CD62L) and n = 3-23 (CCR7) donors. Statistics, as in f. **h**, scRNA-seq-derived UMAP of CD8$^+$ T cells with donor annotation. **i**, scRNA-seq-derived UMAP with annotated Leiden clusters and dot plot with log-normalized expression of cluster-defining genes. Numbers, Leiden clusters. **j**, Log-normalized expression of selected subset-defining genes and scores across Leiden clusters. **k**, Log-normalized expression of selected subset-defining transcription factor networks across Leiden clusters. **l**, Pseudotime of A2/NS4B$^+$CD8$^+$ T cells per Leiden cluster. Clusters are ordered by pseudotime. Dashed line, cut-off for low pseudotime (0.2). **m**, Percentage of cells with low pseudotime (< 0.2) within A2/NS4B$^+$CD8$^+$ T cells per timepoint (left) or Leiden cluster (right).

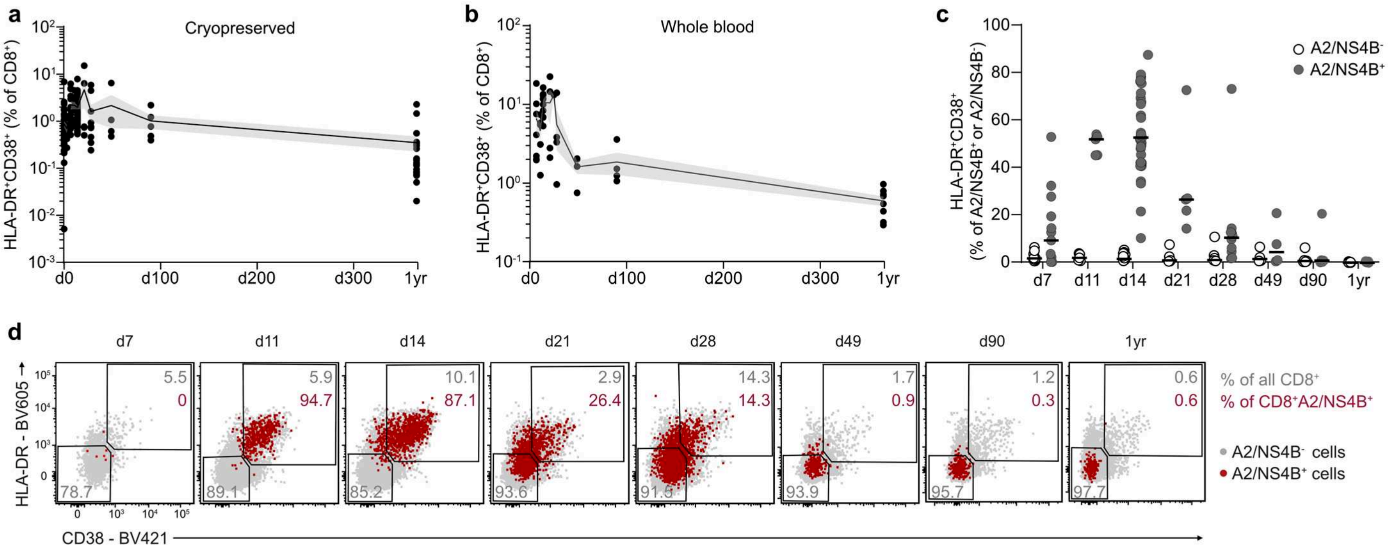

Extended Data Fig. 2 | YFV-specific T cells show transient activation. a,b HLA-DR$^+$CD38$^+$CD8$^+$ T cells in cryopreserved (**a**) and whole blood (**b**) samples by flow cytometry. Solid line, mean. Gray area, SD. n = 4-58 (**a**) and n = 4-11 (**b**) donors. **c**, HLA-DR$^+$CD38$^+$CD8$^+$ T cells in A2/NS4B$^-$CD8$^+$ or A2/NS4B$^+$CD8$^+$ T cells by flow cytometry. Solid line, mean. n = 4-37 donors. **d**, Representative plots for HLA-DR and CD38 expression of T cells in whole blood after vaccination (pregated on living, CD19$^-$CD56$^-$CD4$^-$CD3$^+$CD8$^+$ lymphocytes). Red, A2/NS4B$^+$CD8$^+$ T cells. Gray, A2/NS4B$^-$CD8$^+$ T cells. Red text, percentage of HLA-DR$^+$CD38$^+$ cells among A2/NS4B$^+$CD8$^+$ T cells; Gray text, percentage of HLA-DR$^+$CD38$^+$ (reactive; top right) or HLA-DR$^-$CD38$^-$ (non-reactive; bottom left) among CD8$^+$ T cells.

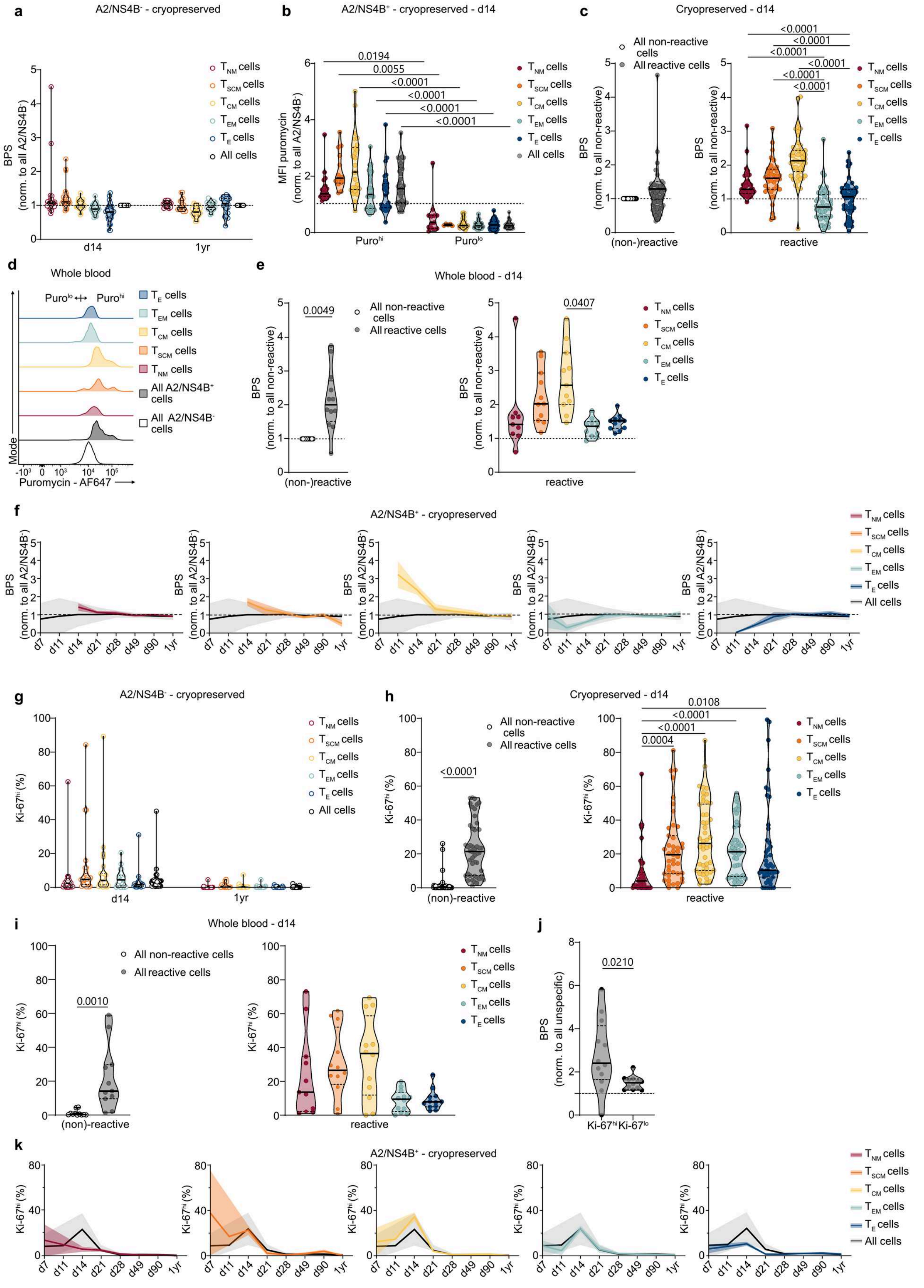

Extended Data Fig. 3 | See next page for caption.

Extended Data Fig. 3 | YFV-specific and -reactive CD8$^+$ T cell subsets undergo metabolic and proliferative dynamics. **a**, Basal protein synthesis (BPS) of A2/NS4B$^-$CD8$^+$ T cell subsets (CD62L$^+$CD45RA$^+$CD95$^-$ T$_{NM}$, CD62L$^+$CD45RA$^+$CD95$^+$ T$_{SCM}$, CD62L$^+$CD45RA$^-$ T$_{CM}$, CD62L$^-$CD45RA$^-$ T$_{EM}$, CD62L$^-$CD45RA$^+$ T$_E$ cells) by flow cytometry, normalized to A2/NS4B$^-$CD8$^+$ T cells. n = 20-35 donors. Statistics, two-way ANOVA with Šídák's multiple comparisons test. **b**, Puromycin incorporation in puro^{hi} and puro^{lo} A2/NS4B$^+$CD8$^+$ T cell subsets (defined in a) on day 14 post-YFV vaccination by flow cytometry. n = 32 donors. Statistics, Kruskal-Wallis test with Dunn's multiple comparisons test. **c**, BPS of HLA-DR$^+$CD38$^+$ (reactive) and HLA-DR$^-$CD38$^-$ (non-reactive) cryopreserved CD8$^+$ T cell subsets (defined in a) on day 14 post-YFV vaccination analyzed by flow cytometry, normalized to non-reactive cells. n = 56 donors. Statistics, (left) two-sided Wilcoxon matched-pairs signed rank test and (right) Kruskal-Wallis test with Dunn's multiple comparisons test. **d,e**, Representative flow cytometry histogram for puromycin incorporation (**d**) and quantification of BPS (**e**) in A2/NS4B$^-$CD8$^+$ and A2/NS4B$^+$CD8$^+$ T cells and A2/NS4B$^+$CD8$^+$ T cell subsets (defined in a) on day 14 post-YFV vaccination in whole blood. Statistics as in c. n = 12 donors. **f**, BPS within A2/NS4B$^+$CD8$^+$ T cell subsets (defined in a) post-YFV vaccination analyzed as in a. Lines, mean. Shaded areas, SEM. n = 2-29 donors. Statistics, two-way ANOVA with Šídák's multiple comparisons test. **g**, Ki-67^{hi} cells within A2/NS4B$^-$CD8$^+$ T cell subsets (defined in a) post-YFV vaccination analyzed by flow cytometry. n = 30 donors. Statistics, two-way ANOVA with Tukey's multiple comparisons test. **h,i** Ki-67^{hi} cells within indicated cryopreserved (**h**) and whole blood (**i**) CD8$^+$ T cell subsets (defined in a) on day 14 post-YFV vaccination. Statistics, as in c. n = 46 (**h**) and n = 11 (**i**) donors. **j**, BPS of Ki-67^{hi} and Ki-67^{lo} A2/NS4B$^+$CD8$^+$ T cells on day 14 post-YFV vaccination analyzed as in a. n = 12 donors. Statistics, two-sided Wilcoxon matched-pairs signed rank test. **k**, Ki-67^{hi} cells within A2/NS4B$^+$CD8$^+$ T cell subsets (defined in a) after YFV vaccination. Lines, mean. Shaded areas, SEM. n = 2-29 donors.

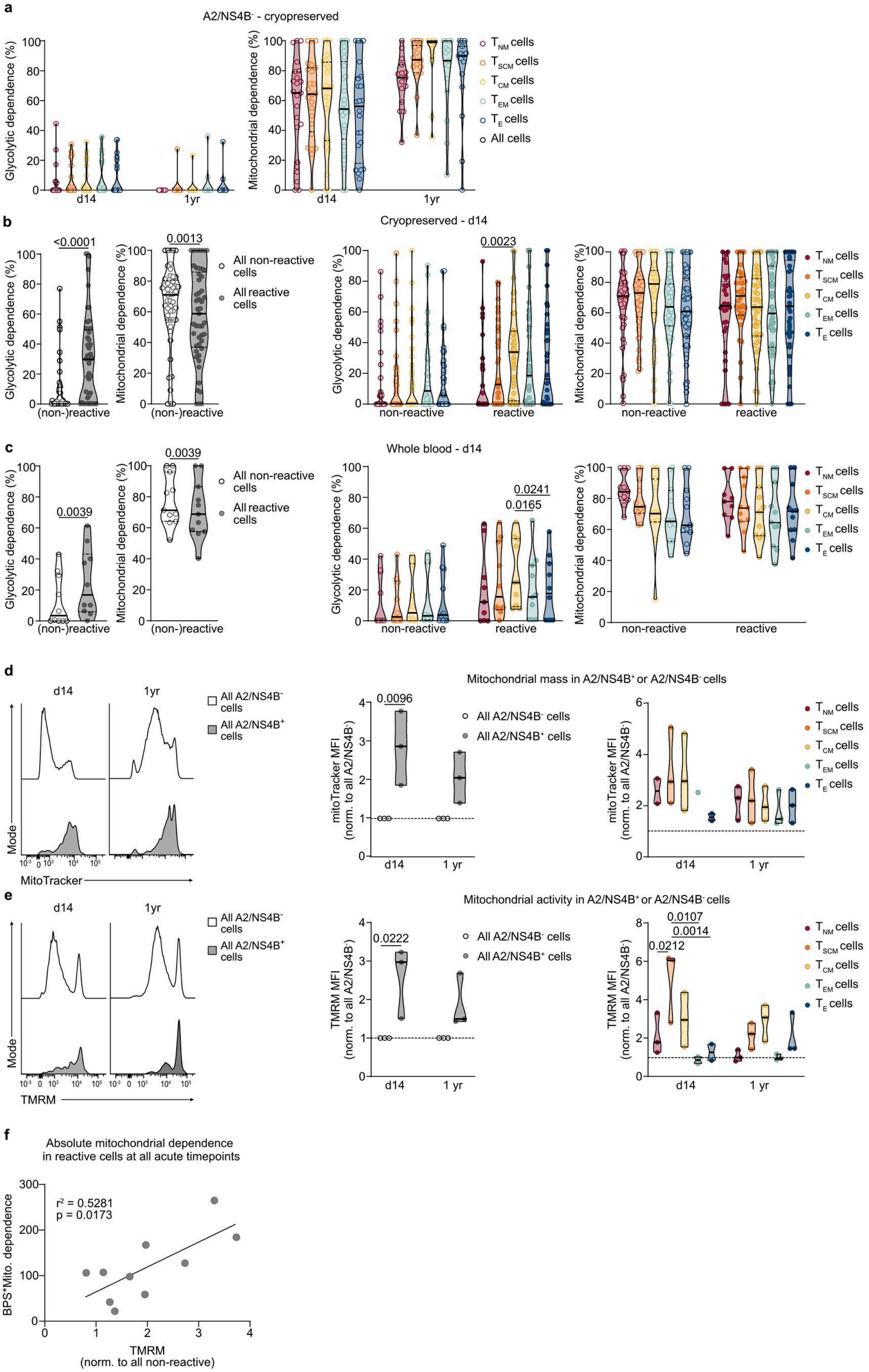

Extended Data Fig. 4 | See next page for caption.

Extended Data Fig. 4 | YFV-specific and reactive CD8$^+$ T cell subsets show distinct metabolic dependencies. a, Glycolytic (left) and mitochondrial (right) dependence determined by SCENITH in cryopreserved A2/NS4B$^-$CD8$^+$ T cell subsets (CD62L$^+$CD45RA$^+$CD95$^-$ T$_{NM}$, CD62L$^+$CD45RA$^+$CD95$^+$ T$_{SCM}$, CD62L$^+$CD45RA$^-$ T$_{CM}$, CD62L$^-$CD45RA$^-$ T$_{EM}$, CD62L$^-$CD45RA$^+$ T$_E$ cells). n = 14-34 donors. Statistics, two-way ANOVA with Šídák's multiple comparisons test. **b,c**, Glycolytic and mitochondrial dependence determined by SCENITH in indicated, cryopreserved (**b**) and whole blood samples (**c**) in all HLA-DR$^+$CD38$^+$CD8$^+$ (reactive), HLA-DR$^-$CD38$^-$CD8$^+$ (non-reactive) (left) and HLA-DR$^+$CD38$^+$CD8$^+$ T cell subsets (defined in a; right) on day 14 post-YFV vaccination. Statistics, two-sided Wilcoxon matched-pairs signed rank test (left) and Kruskal-Wallis test with Dunn's multiple comparisons test (right). n = 44-59 (**b**) and n = 10-11 (**c**) donors. **d,e**, Representative flow cytometry histograms for mitoTrackerGreen (**d**) and TMRM (**e**) staining in A2/NS4B$^-$CD8$^+$ and A2/NS4B$^+$CD8$^+$ T cells and quantifications for A2/NS4B$^-$CD8$^+$ and A2/NS4B$^+$CD8$^+$ T cells or A2/NS4B$^+$CD8$^+$ T cell subsets (defined in a) post-YFV vaccination analyzed by flow cytometry. Statistics, two-way ANOVA with Šídák's multiple comparisons test (left) and Mixed-effects analysis with Tukey's multiple comparisons test (right). n = 3 donors. **f**, Correlation of mitochondrial activity determined by TMRM and absolute mitochondrial dependence from SCENITH (Basal protein synthesis (BPS) multiplied with mitochondrial dependence) in reactive CD8$^+$ T cells in the effector phase (day 7, 11, 14 after YFV vaccination combined). The correlation coefficient was computed as two-sided Pearson correlation coefficient. Dots, donors. n = 10 donors.

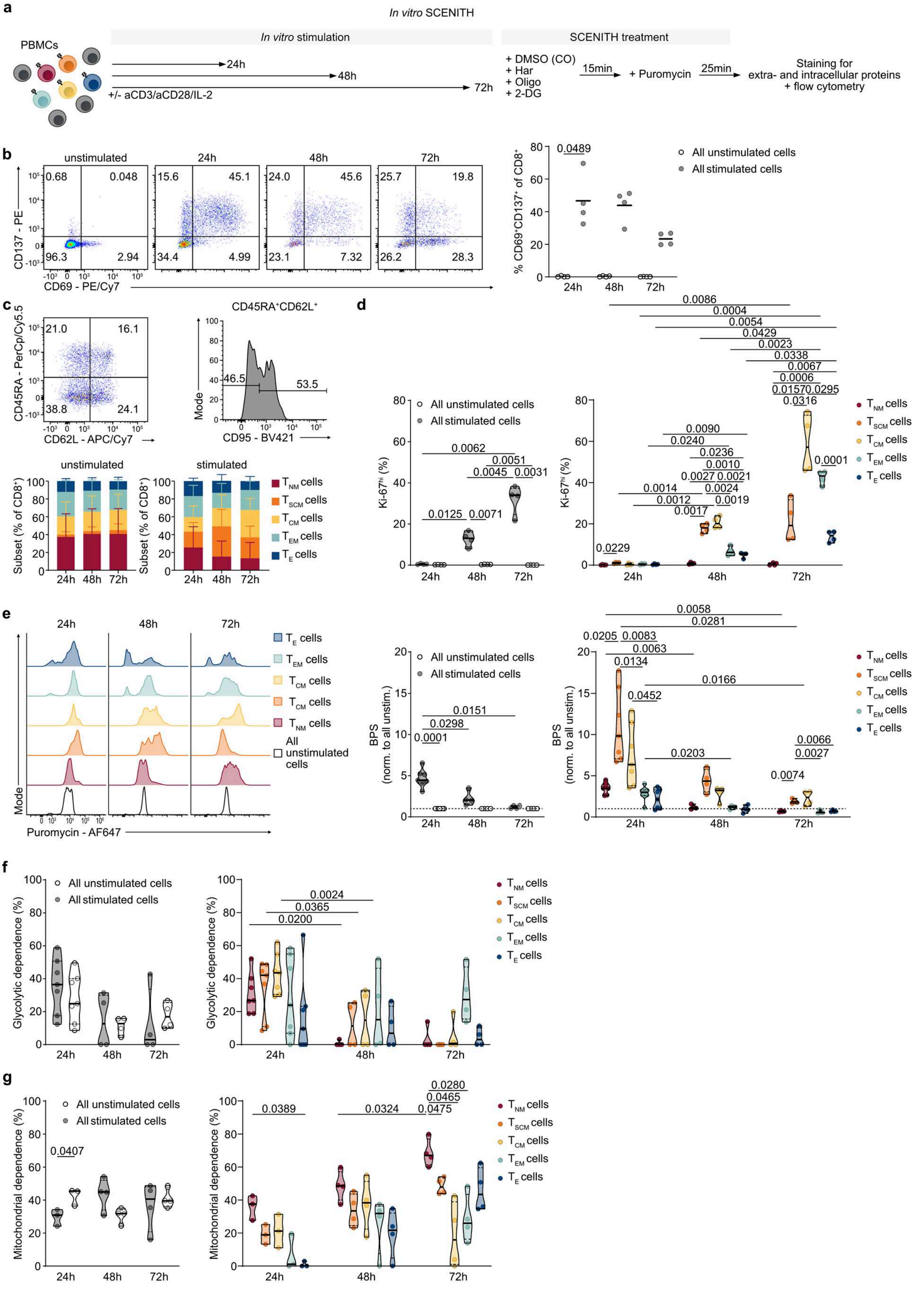

Extended Data Fig. 5 | See next page for caption.

Extended Data Fig. 5 | Polyclonal CD8$^+$ T cells undergo metabolic rewiring after *in-vitro* stimulation. **a**, Experimental setup for *in vitro* SCENITH. **b**, CD137$^+$CD69$^+$ cells in unstimulated CD8$^+$ T cells and 24h-, 48h-, 72h-stimulated CD8$^+$ T cells determined by flow cytometry (pregated on living, CD19$^-$CD56$^-$CD4$^-$ lymphocytes). Bold lines, mean. Statistics, Friedman test with Dunn's multiple comparisons test. 24 h, 48 h, 72 h, n = 4 donors from one experiment. **c**, Representative plots of 24h-stimulated CD8$^+$ T cells (top) and quantification over time (bottom) showing subsets (CD62L$^+$CD45RA$^+$CD95$^-$ T_{NM}, CD62L$^+$CD45RA$^+$CD95$^+$ T_{SCM}, CD62L$^+$CD45RA$^-$ T_{CM}, CD62L$^-$CD45RA$^-$ T_{EM}, CD62L$^-$CD45RA$^+$ T_E cells) of CD8$^+$ T cells after *in vitro* culture with or without stimulus determined by flow cytometry. Bars, mean and SEM. 24 h, n = 7 from two individual experiments; 48 h, 72 h, n = 4 donors from one experiment. **d**, Ki-67^{hi} cells in unstimulated and stimulated CD8$^+$ T cells (left) or stimulated CD8$^+$ T cell subsets (defined in c; right) determined by flow cytometry. Statistics, two-way ANOVA with Tukey's multiple comparisons test. Donors as in b. **e**, Representative histograms for puromycin incorporation (left) and quantification of basal protein synthesis (BPS) for CD8$^+$ T cells (middle) or stimulated CD8$^+$ T cell subsets (defined in c; right) normalized to unstimulated CD8$^+$ T cells. Statistics, two-way ANOVA with Šídák's multiple comparisons test (middle) and Tukey's multiple comparisons test (right). Donors as in c. **f**, Glycolytic dependence determined by SCENITH for unstimulated and stimulated CD8$^+$ T cells (left) or stimulated CD8$^+$ T cell subsets (defined in c; right). Statistics, two-way ANOVA with Šídák's multiple comparisons test. Donors as in c. **g**, Mitochondrial dependence determined and depicted as in f. 24 h, n = 3 donors; 48 h, 72 h, n = 4 donors from one experiment.

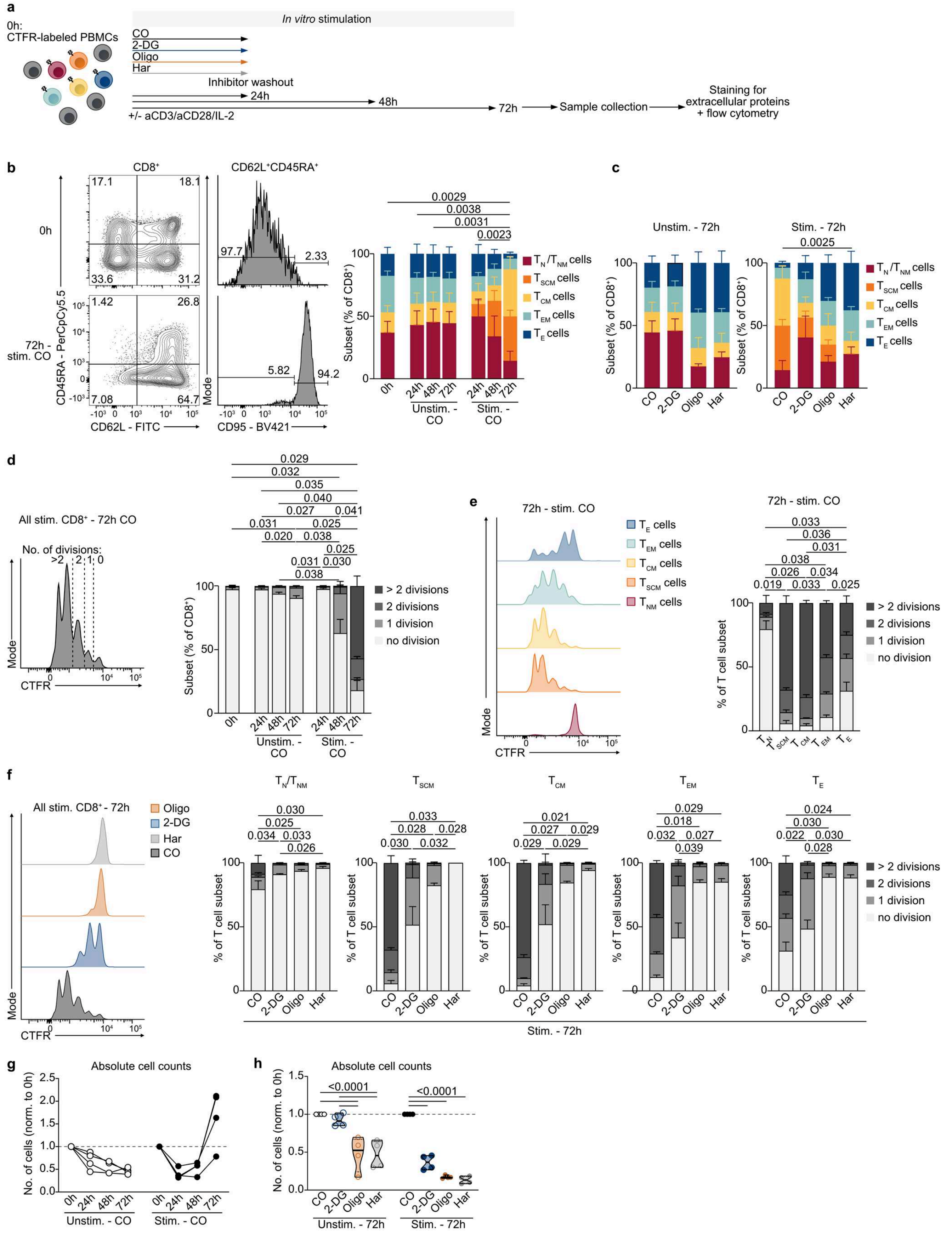

Extended Data Fig. 6 | See next page for caption.

Extended Data Fig. 6 | Differentiation and proliferation of CD8$^+$ T cells are dependent on metabolic pathways after *in-vitro* stimulation. a, Experimental setup for the *in vitro* proliferation assay with metabolic perturbations. **b**, Representative plots (left) and quantification (right) of CD8$^+$ T cell subsets (CD62L$^+$CD45RA$^+$CD95$^-$ T_{NM}, CD62L$^+$CD45RA$^+$CD95$^+$ T_{SCM}, CD62L$^+$CD45RA$^-$ T_{CM}, CD62L$^-$CD45RA$^-$ T_{EM}, CD62L$^-$CD45RA$^+$ T_E cells) pregated on living, CD19$^-$CD56$^-$CD4$^-$CD8$^+$ lymphocytes in CO samples before stimulation (0 h) or after incubation with or without stimulation as indicated. Bars, mean and SEM. Statistics, two-sided permanova comparing shown conditions among each other (2 groups per comparison, 999 permutations). n = 4 donors from one experiment. **c**, CD8$^+$ T cell subsets (defined in b) after 72 h with or without stimulation and with or without metabolic perturbations as determined in b. Bars, mean and SEM. Statistics and donors as in b. **d**, Representative plot (left) and quantification (right) of cell divisions in CD8$^+$ T cells in indicated conditions by CTFR in flow cytometry. Bars, mean and SEM. Statistics and donors as in b. **e**, Cell divisions in T cell subsets (defined in b) of the CO samples after 72 h of stimulation, analyzed as in d. Statistics and donors as in b. **f**, Representative plot (left) and quantification (right) showing cell divisions in CD8$^+$ T cells and CD8$^+$ T cell subsets (defined in b) after 72 h of stimulation with or without metabolic perturbations, analyzed as in d. Bars, mean and SEM. Statistics and donors as in b. **g,h** Absolute numbers of CD8$^+$ T cells in CO samples at indicated timepoints (**g**) and inhibitor-treated samples after 72 h without or with stimulation determined by flow cytometry. Counts were normalized to cell counts at 0 h (**g**) or cell counts in the respective CO samples (**h**). Donors as in b. (**g**) Lines connect datapoints derived from the same donor. (**h**) Statistics, two-way ANOVA with Šídák's multiple comparisons test.

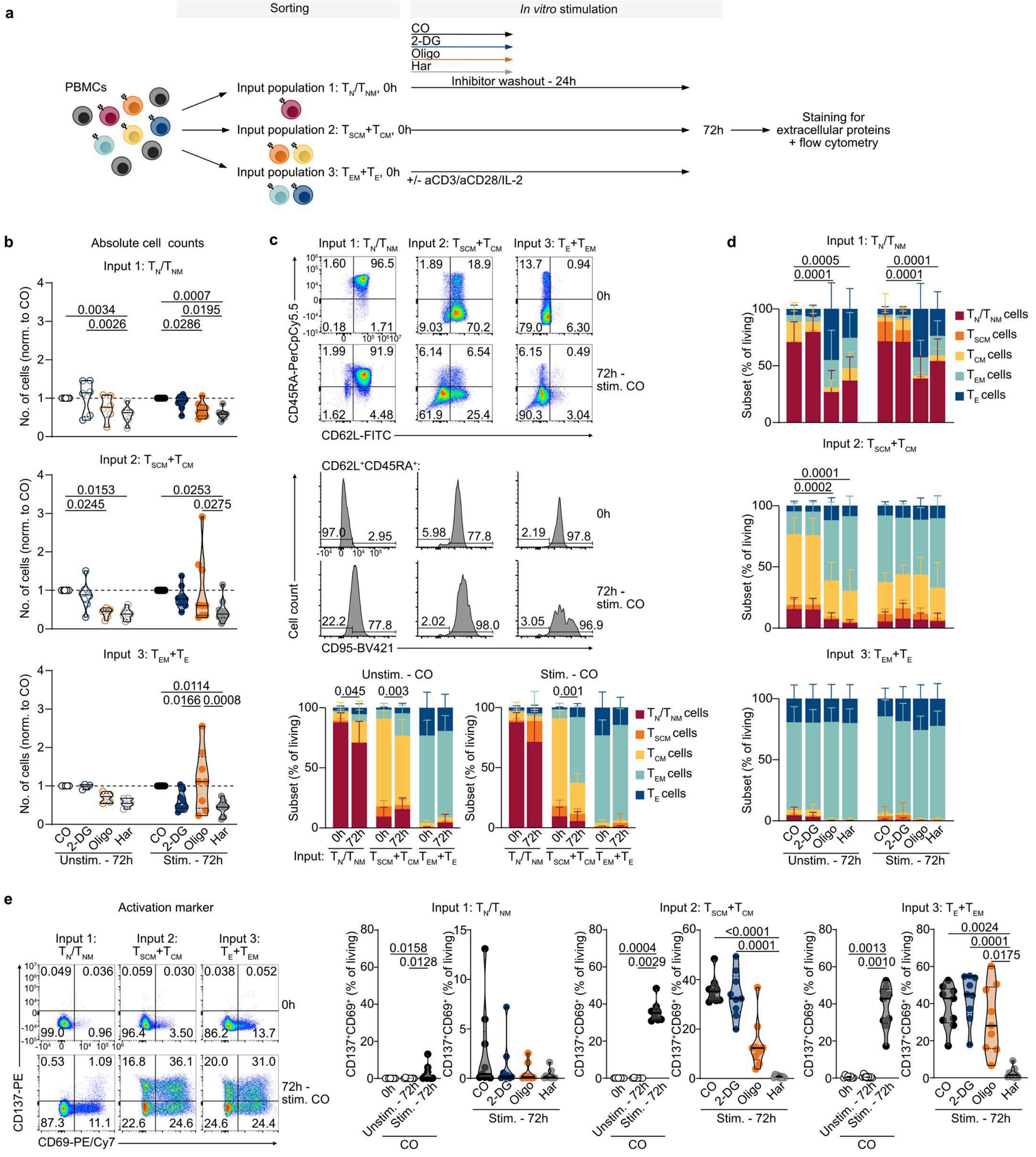

Extended Data Fig. 7 | See next page for caption.

Extended Data Fig. 7 | Sorted CD8$^+$ T cell subsets show unique differentiation, proliferation and activation after metabolic perturbations and *in vitro* stimulation. a, Experimental setup for the *in vitro* stimulation assay with sorted CD8$^+$ T cell subsets (CD62L$^+$CD45RA$^+$CD95$^-$ T$_{NM}$, CD62L$^+$CD45RA$^+$CD95$^+$ T$_{SCM}$, CD62L$^+$CD45RA$^-$ T$_{CM}$, CD62L$^-$CD45RA$^-$ T$_{EM}$, CD62L$^-$CD45RA$^+$ T$_E$ cells) as input. **b**, Absolute cell counts of living unstimulated and stimulated lymphocytes with and without metabolic perturbation for the indicated sorted input CD8$^+$ T cell subsets (defined in a) determined by flow cytometry. Counts were normalized to the respective CO samples. n = 9 donors from two experiments. Statistics, two-way ANOVA with Tukey's multiple comparisons test. **c**, T cell subset (defined in a) distribution among living lymphocytes in the indicated sorted input populations before stimulation (0 h) or in CO samples after 72 h of incubation with or without stimulation analyzed by flow cytometry. Representative plots (top, middle) and quantification (bottom) over time and input population as indicated. Bars, mean and SEM. n = 9 donors from two experiments. Statistics, two-sided permanova comparing the timepoints for each input population (2 groups, 999 permutations). **d**, T cell subset (defined in a) distribution among living lymphocytes determined as in c after 72 h with or without stimulation in the presence or absence of metabolic perturbations. Bars, mean and SEM. n = 9 donors from two experiments. Statistics, two-sided permanova comparing the metabolic perturbations within each input population and stimulation condition among each other (2 groups per comparison, 999 permutations). **e**, Representative plots (left) and quantification (right) of CD69 and CD137 expression in living lymphocytes of the sorted input populations before stimulation (0 h) or in 72h-stimulated or unstimulated cells with and without metabolic perturbations determined by flow cytometry. n = 9 donors from two experiments. Statistics, Kruskal-Wallis test with Dunn's multiple comparisons test.

https://doi.org/10.1038/s41590-026-02421-w

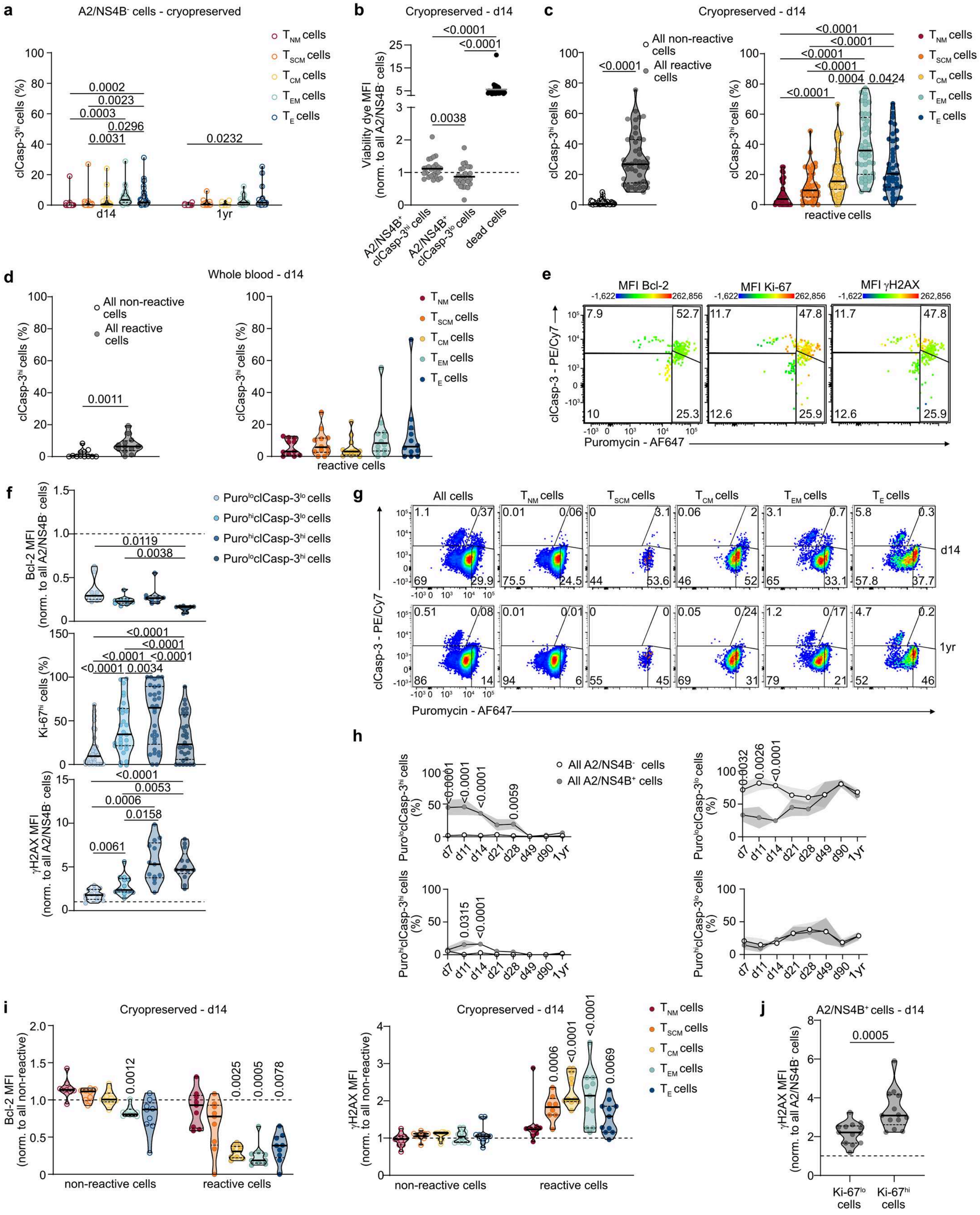

Extended Data Fig. 8 | See next page for caption.

Extended Data Fig. 8 | CD8$^+$ T cell phenotypic subsets contain metabolic subpopulations. a, clCasp-3 expression in A2/NS4B$^-$CD8$^+$ T cell subsets (CD62L$^+$CD45RA$^+$CD95$^-$ T$_{NM}$, CD62L$^+$CD45RA$^+$CD95$^+$ T$_{SCM}$, CD62L$^+$CD45RA$^-$ T$_{CM}$, CD62L$^-$CD45RA$^-$ T$_{EM}$, CD62L$^-$CD45RA$^+$ T$_{E}$ cells) post-YFV vaccination by flow cytometry. n = 20-38 donors. Statistics, two-way ANOVA with Šídák's multiple comparisons test. **b**, Viability dye staining in cryopreserved A2/NS4B$^+$clCasp-3^{hi}CD8$^+$, A2/NS4B$^+$clCasp-3^{lo}CD8$^+$ T cells and dead cells (viability dye^{hi}CD4$^-$CD56$^-$CD19$^-$CD8$^+$ lymphocytes) at day 14 post-YFV vaccination. n = 25 donors. Line, median. Statistics, two-sided tailed Friedman test. **c,d**, clCasp-3 expression in CD38$^-$HLA-DR$^-$CD8$^+$ (non-reactive) and CD38$^+$HLA-DR$^+$CD8$^+$ (reactive) T cells (left) and CD38$^+$HLA-DR$^+$CD8$^+$ T cell subsets (defined in a; right) on day 14 post-YFV vaccination analyzed by flow cytometry in cryopreserved samples (**c**) and whole blood samples (**d**). (**c**) n = 46; (**d**) n = 12 donors. Statistics, two-sided paired t-test (left) and Kruskal-Wallis test with Dunn's multiple comparisons test (right). **e,f**, Representative plot (**e**) and quantification (**f**) for Bcl-2, Ki-67 and yH2AX in A2/NS4B$^+$CD8$^+$ T cell metabolic subpopulations (based on clCasp-3 and puromycin) from cryopreserved samples on day 14 post-YFV vaccination. Bcl-2 and yH2AX MFI were normalized to A2/NS4B$^-$CD8$^+$ T cells. n = 9-30 donors. Statistics, one-way ANOVA with Tukey's multiple comparisons test. **g,h**, Representative gating for metabolic subpopulations in A2/NS4B$^-$CD8$^+$ T cells subsets (defined in a) (**g**) and quantification of metabolic subpopulations (**h**) within A2/NS4B$^-$CD8$^+$ and A2/NS4B$^+$CD8$^+$ T cells in cryopreserved samples post-YFV vaccination. Lines, mean. Shaded areas, SEM. Statistics, two-way ANOVA with Tukey's multiple comparisons test. Statistically significant differences over time for: Puro^{lo}clCasp3^{lo}, Puro^{hi}clCasp3^{hi}, Puro^{lo}clCasp3^{hi} cells. n = 4-38 donors. **i**, Expression of BCLl-2 (left) and yH2AX (right) in non-reactive and reactive T cell subsets (defined in a) on day 14 post-YFV vaccination in cryopreserved samples by flow cytometry, normalized to non-reactive CD8$^+$ T cells. n = 9 (left); n = 11 (right) donors. Statistics, Kruskal-Wallis test with Dunn's multiple comparisons test (each subset (defined in a) against non-reactive CD8$^+$ T cells). **j**, Expression of yH2AX in cryopreserved Ki-67^{hi} and Ki-67^{lo}A2/NS4B$^+$CD8$^+$ T cells on day 14 post-YFV vaccination, normalized to A2/NS4B$^-$CD8$^+$ T cells. n = 13 donors. Statistics, two-sided paired t-test.

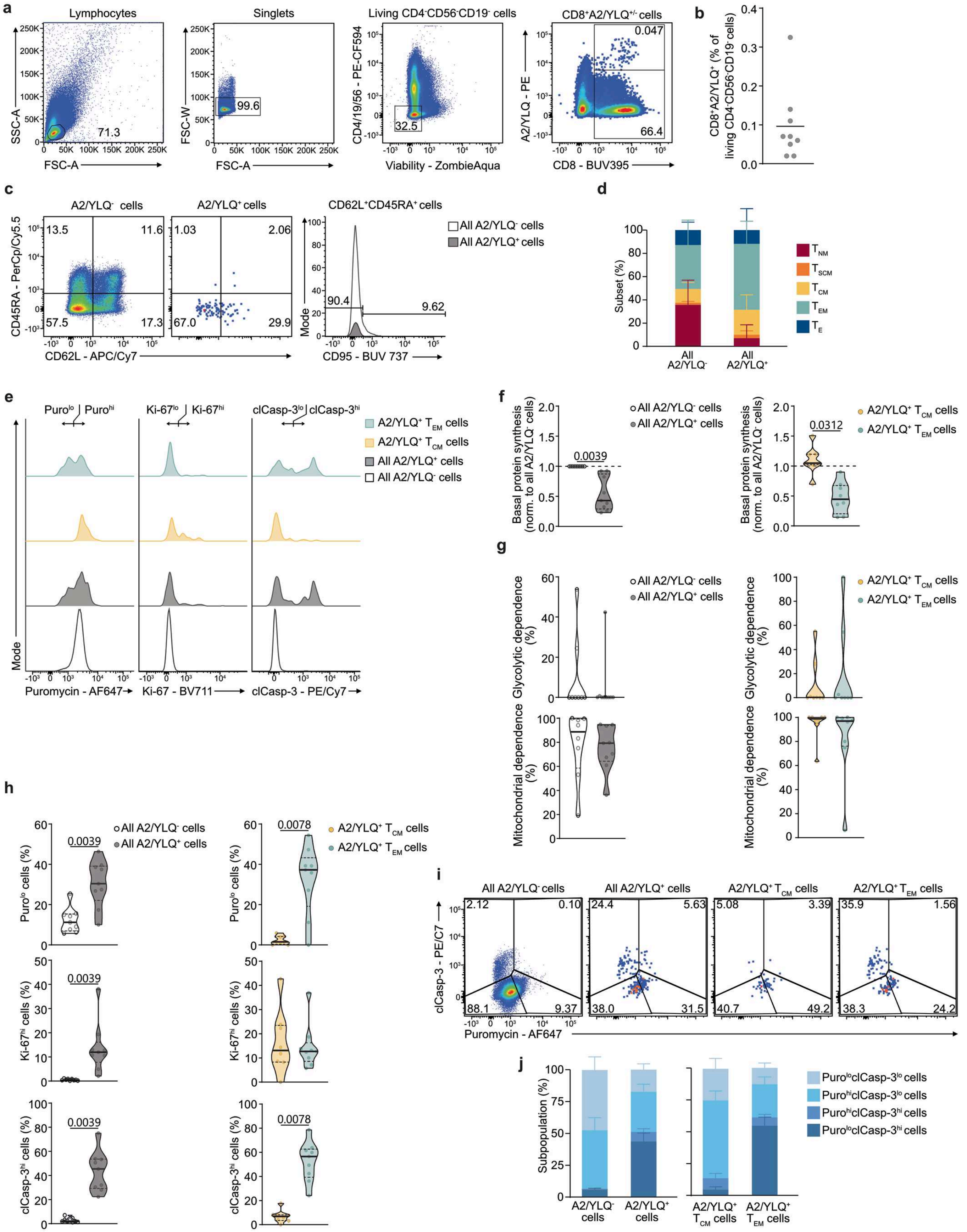

Extended Data Fig. 9 | See next page for caption.

Extended Data Fig. 9 | Metabolic features are conserved in SARS-CoV-2-specific central and effector memory CD8$^+$ T cells. a, Representative gating of A2/YLQ$^-$CD8$^+$ and A2/YLQ$^+$CD8$^+$ T cells on day 10 after second SARS-CoV-2 vaccination. **b**, A2/YLQ$^+$CD8$^+$ T cells on day 10 after second SARS-CoV-2 vaccination determined as in a. n = 9 donors. Line, mean. **c**, Representative gating of A2/YLQ$^-$CD8$^+$ and A2/YLQ$^+$CD8$^+$ T cell subsets on day 10 after second SARS-CoV-2 vaccination (pregated as in a). **d**, A2/YLQ$^-$CD8$^+$ and A2/YLQ$^+$CD8$^+$ T cell subsets (CD62L$^+$CD45RA$^+$CD95$^-$ T$_{NM}$, CD62L$^+$CD45RA$^+$CD95$^+$ T$_{SCM}$, CD62L$^+$CD45RA$^-$ T$_{CM}$, CD62L$^-$CD45RA$^-$ T$_{EM}$ and CD62L$^-$CD45RA$^+$ effector T$_E$ cells) analyzed as in c. Bars, mean and SEM. n = 9 donors. **e**, Representative histograms for puromycin incorporation, Ki-67 and clCasp-3 expression in the indicated CD8$^+$ T cell subsets (defined in d) on day 10 after second SARS-CoV-2 vaccination, analyzed by flow cytometry. **f**, Basal protein synthesis (BPS) in the indicated CD8$^+$ T cell subsets (defined in d) on day 10 after second SARS-CoV-2 vaccination analyzed by SCENITH. BPS was normalized to A2/YLQ$^-$CD8$^+$ T cells. n = 9 donors. Statistics, two-sided Wilcoxon test. **g**, Glycolytic (top) and mitochondrial (bottom) dependence of indicated CD8$^+$ T cell subsets (defined in d) on day 10 after second SARS-CoV-2 vaccination analyzed by SCENITH. n = 9 donors. Statistics, two-sided Wilcoxon test. **h**, Percentages of Puro^{lo}, Ki-67^{hi} and clCasp-3^{hi} cells among the indicated CD8$^+$ T cell subsets (defined in d) on day 10 after second SARS-CoV-2 vaccination analyzed by flow cytometry. Statistics, two-sided Wilcoxon test. **i,j** Representative flow cytometry plots (**i**) and quantification (**j**) for metabolic subpopulations (based on clCasp-3 and puromycin) in the indicated CD8$^+$ T cell subsets (defined in d) on day 10 after second SARS-CoV-2 vaccination. Bars, mean and SEM. n = 9 donors.

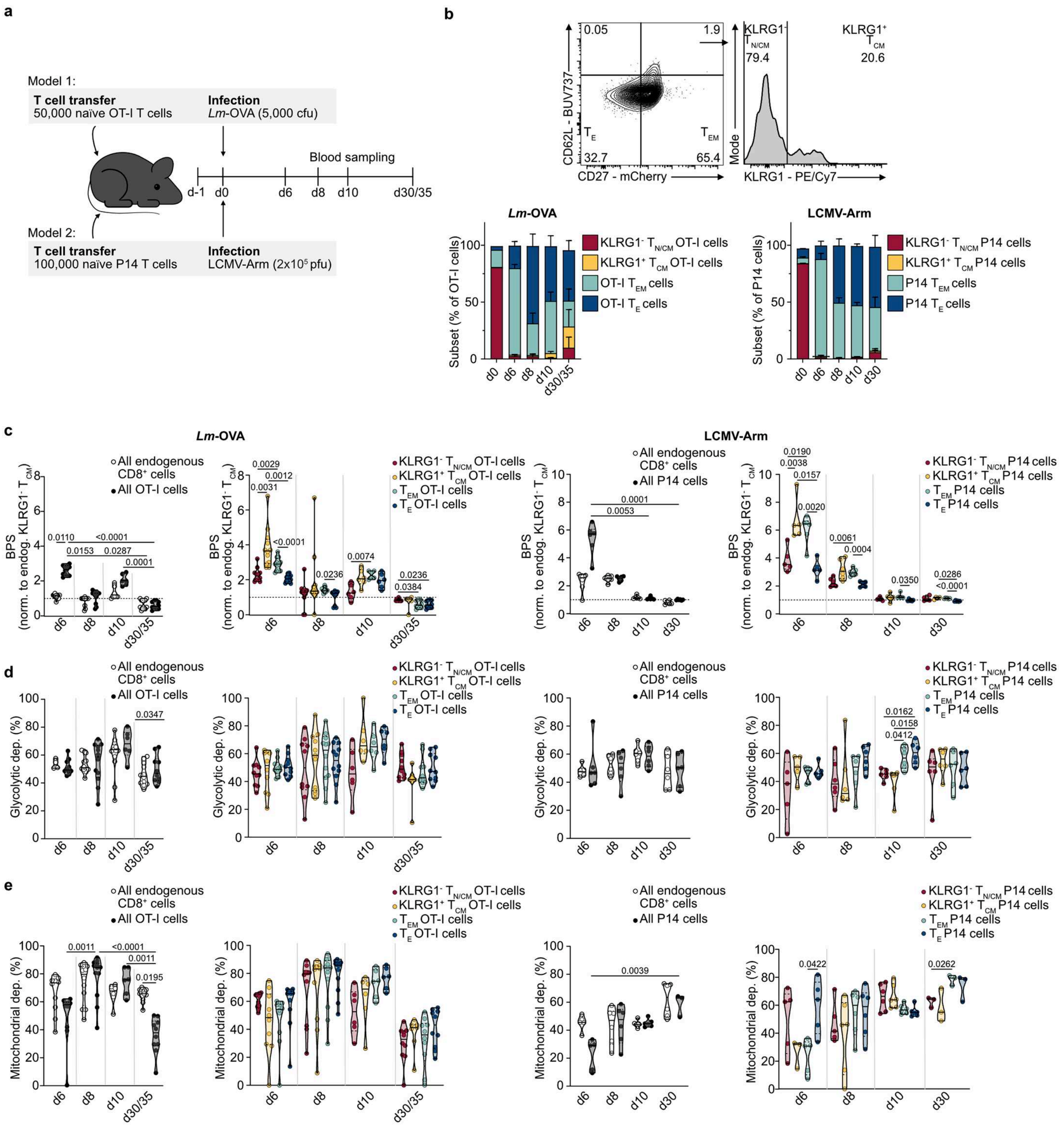

Extended Data Fig. 10 | Antigen-specific mouse CD8$^+$ T cells show conserved metabolic activities but divergent dependencies compared to human T cells. **a**, Schematics for the two infection models of murine antigen-specific T cell responses. *Lm*-OVA, OVA-expressing *Listeria monocytogenes*; cfu, colony-forming units; LCMV-Arm, LCMV-Armstrong; pfu, plaque-forming units. *Lm*-OVA infection, two individual experiments with a total of 10-12 mice (day 6, 8, 30/35) or one experiment with six mice (day 10). LCMV-Arm infection, one experiment with six mice (day 6, 8, 30). **b**, Representative flow cytometry plots (top) for the identification of phenotypic subsets (CD27$^+$CD62L$^+$KLRG1$^-$ T$_{N/CM}$, CD27$^+$CD62L$^+$KLRG1$^+$ T$_{CM}$, CD27$^+$CD62L$^-$ T$_{EM}$ and CD27$^-$CD62L$^-$ T$_E$ cells) within antigen-specific OT-I T cells on d6 post *Lm*-OVA infection and quantification (bottom) across all mice and timepoints after infection; day 0 represents the subset composition of OT-I and P14 T cells after isolation from the spleen of donor mice and before T cell transfer into recipients. Cells were pre-gated on CD8$^+$CD4$^-$CD45.1$^+$ single lymphocytes for transferred T cells or CD8$^+$CD4$^-$CD45.1$^-$ single lymphocytes for endogenous T cells. **c**, Basal protein synthesis (BPS) in endogenous CD8$^+$ or OT-I T cells (left) and OT-I T cell subsets (as defined in b, middle left) after *Lm*-OVA infection or endogenous CD8$^+$ and P14 T cells (middle right) and P14 T cell subsets (left) at the indicated timepoints after infection determined by SCENITH. BPS was normalized to endogenous CD8$^+$CD27$^+$CD62L$^+$KLRG1$^-$ T$_{CM}$ cells. Statistics, Kruskal-Wallis test with Dunn's multiple comparisons test (left, middle right); mixed-effects analysis with Tukey's multiple comparisons test (middle left, right). **d**, Glycolytic dependence determined by SCENITH displayed as in c. Statistics, as in c. **e**, Mitochondrial dependence determined by SCENITH displayed as in c. Statistics, as in c.